**An Empirical Prediction Model of the Performance
Impacts of Material Tolerances in Frequency
Selective Surfaces using the Monte Carlo Method**

Matthew D. Craig
AFIT/GE/ENG/99M-05

19990413 096

# REPORT DOCUMENTATION PAGE

Public reporting burden for this collection of information is estimated to average 1 hour per response, including the time for reviewing instructions, searching existing data sources, gathering and maintaining the data needed, and completing and reviewing the collection of information. Send comments regarding this burden estimate or any other aspect of this collection of information, including suggestions for reducing this burden, to Washington Headquarters Services, Directorate for Information Operations and Reports, 1215 Jefferson Davis Highway, Suite 1204, Arlington, VA 22202-4302, and to the Office of Management and Budget, Paperwork Reduction Project (0704-0188), Washington, DC 20503.

| 1. AGENCY USE ONLY *(Leave blank)* | 2. REPORT DATE<br>March 1999 | 3. REPORT TYPE AND DATES COVERED<br>Master's Thesis | |
|---|---|---|---|

**4. TITLE AND SUBTITLE**
An Empirical Prediction Model of the Performance Impacts of Material Tolerances in Frequency Selective Surfaces using the Monte Carlo Method

**5. FUNDING NUMBERS**

**6. AUTHOR(S)**
MATTHEW D. CRAIG, Captain, USAF

**7. PERFORMING ORGANIZATION NAME(S) AND ADDRESS(ES)**
Air Force Institute of Technology (AFIT)
2950 P Street
Wright-Patterson AFB, OH 45433-7765

**8. PERFORMING ORGANIZATION REPORT NUMBER**

AFIT/GE/ENG/99M-05

**9. SPONSORING/MONITORING AGENCY NAME(S) AND ADDRESS(ES)**
AFRL/XPN
2591 K ST
WRIGHT-PATTERSON AFB   OH 45433-7602
Mr. Edwin L. Utt, Principal Electrical Engineer
(937) 255-0276

**10. SPONSORING/MONITORING AGENCY REPORT NUMBER**

**11. SUPPLEMENTARY NOTES**
Advisor: Major Peter J. Collins
(937) 255-6565 ext. 4304
email: Peter.Collins@afit.af.mil

**12a. DISTRIBUTION AVAILABILITY STATEMENT**
Approved for public release; distribution unlimited

**12b. DISTRIBUTION CODE**

**13. ABSTRACT** *(Maximum 200 words)*

Standard computational tools predicting frequency selective surface (FSS) performance model periodic structures as an infinite-by-infinite array of perfectly placed elements with perfect, identical dimensions, and with dielectric layers of uniform thickness and material composition. These models do not address perturbations caused by manufacturing tolerances of elements and dielectric layers, nor do they address edge effects caused by finite-by-finite dimensional arrays. The Monte Carlo Method was used to determine the effects of random variations in element dimension, placement, dielectric thickness, and dielectric material on FSS performance. A full-factorial experimental design was applied, and eight hundred twenty-five unique finite arrays of elements were generated with dimensions that varied randomly within tolerances. Each array was analyzed using the AIM code (Adaptive Integral Method), and a sensitivity analysis was performed to determine the influence of design parameter tolerances on FSS performance. Dipole length was shown to have the most significant impact on FSS performance. Dielectric material constant, and the combination of dipole length and dipole placement in the "length" direction also had statistically significant impact on FSS performance. In addition, low tolerances for two design parameter combinations--dielectric thickness alone, and the combination of all five design parameters--produced significant rapid variation in output performance data.

| 14. SUBJECT TERMS<br>Frequency selective surface, antenna array, antenna, radome, tolerance, Monte Carlo, Moment Method, computational electromagnetics, Adaptive Integral Method, AIM | 15. NUMBER OF PAGES<br>95 |
|---|---|
| | 16. PRICE CODE |

| 17. SECURITY CLASSIFICATION OF REPORT<br>Unclassified | 18. SECURITY CLASSIFICATION OF THIS PAGE<br>Unclassified | 19. SECURITY CLASSIFICATION OF ABSTRACT<br>Unclassified | 20. LIMITATION OF ABSTRACT<br>UL |
|---|---|---|---|

# An Empirical Prediction Model of the Performance Impacts of Material Tolerances in Frequency Selective Surfaces using the Monte Carlo Method

THESIS

Presented to the faculty of the Graduate School of Engineering

of the Air Force Institute of Technology

In Partial Fulfillment of the

Requirements for the Degree of

Master of Science in Electrical Engineering

Matthew D. Craig

Captain, USAF

March, 1999

AFIT/GE/ENG/99M-05

**An Empirical Prediction Model of the Performance Impacts of Material Tolerances**

**in Frequency Selective Surfaces using the Monte Carlo Method**

Matthew D. Craig

Captain, USAF

Approved:

_____     _____

Peter J. Collins, PhD, Major, Committee Chairman               Date

Department of Electrical and Computer Engineering

_____     _____

Andrew J. Terzouli, Jr., PhD, Committee Member               Date

Department of Electrical and Computer Engineering

_____     _____

Lawrence K. Chilton, PhD, Lieutenant Colonel, Committee Member     Date

Department of Mathematics and Statistics

# Acknowledgments

The research recorded in this thesis would not have been possible without the unceasing support of my wife, Tracy, who provided constant encouragement when I encountered frustration and difficulty. Her dedication, understanding, and humor transformed the work behind this research effort from tolerable to enjoyable.

I would like to thank Major Peter J. Collins, my thesis advisor, for delivering precision technical knowledge where and when I needed it. I am indebted to committee members Dr. Andrew Terzouli and Lieutenant Colonel Lawrence Chilton, for their understanding of electromagnetics and numerical methods, respectively. Invaluable statistics and experimental design guidance was provided by Captain Samuel Gardner, and Major Bill Wood of AFRL/XPN provided key advice regarding the AIM code.

Finally, a deep thanks goes out to my fellow classmates in the AFIT Low Observables program: Captains Grayson Cochran, Bob Eigel, Art Ford, and Karl Schloer. They helped to lessen the shock of a physicist placed in an electrical engineering program with patience and knowledge.

<div align="right">Matthew D. Craig</div>

TABLE OF CONTENTS

**TABLE OF FIGURES**

**ABSTRACT**

Standard computational tools predicting frequency selective surface (FSS) performance model periodic structures as an infinite-by-infinite array of perfectly placed elements with perfect, identical dimensions, and with dielectric layers of uniform thickness and material composition. These models do not address perturbations caused by manufacturing tolerances of elements and dielectric layers, nor do they address edge effects that occur in finite-by-finite dimensional arrays. The Monte Carlo Method was used to determine the effects of random variations in element dimension, placement, dielectric thickness, and dielectric material on FSS performance. A full-factorial experimental design was applied, and eight hundred unique finite arrays of elements were generated with dimensions that varied randomly within tolerances. Each array was analyzed using the AIM code (Adaptive Integral Method), and a sensitivity analysis was performed to determine the influence of design parameter tolerances on FSS performance. Dipole length was shown to have the most significant impact on FSS performance. Dielectric material constant, and the combination of dipole length and dipole placement in the "length" direction also had statistically significant impact on FSS performance. In addition, low tolerances for two design parameter combinations-- dielectric thickness alone, and the combination of all five design parameters--produced significant rapid variation in output performance data.

# An Empirical Prediction Model of the Performance Impacts of Material Tolerances in Frequency Selective Surfaces using the Monte Carlo Method

## 1 INTRODUCTION

### 1.1 Problem Statement

A frequency selective surface (FSS) is a periodic structure that acts as a bandstop or bandpass filter, depending on the user's application. For example, the reflector dish of an antenna may consist of a frequency selective surface, designed to reflect radiation at the antenna's operating frequency. Similarly, a radome may have a FSS embedded within its shell that allows only certain frequencies through, appearing electrically opaque to all other frequencies.

All frequency selective surfaces are composed of an array of elements, which are geometric structures designed to reflect or absorb electromagnetic energy at certain frequencies. The geometry of these elements can vary widely, and include rectangular slots, dipoles, tripoles, and crosses [Munk]. These elements may be printed on a dielectric, machined into a ground plane, sandwiched between layers of dielectric, or any

of a multitude of other configurations. The surfaces upon which the elements reside come in a variety of geometric shapes, but are usually flat, cone-shaped, or dome-shaped.

A standard tool for FSS design has been Henderson's Periodic Moment Method code (PMM), which models the FSS as an infinite-by-infinite array of identically shaped, perfectly placed elements. This infinite periodicity allows the application of Floquet's Theorem, which states that an incident plane wave will produce identical scattered fields from each element, with an appropriate phase shift; thus, a moment method solution for the impressed surface currents must only be computed for a single element. Floquet's theorem significantly reduces the computational burden of calculating the scattered fields, since the contribution of each element may be treated as equal in magnitude but with a phase shift introduced.

When Floquet's theorem is not applied, the computational resources (memory and CPU time) increase dramatically. This is because each element will have its own unique scattering currents, and accordingly will couple with other elements uniquely. In this case, the moment method must be applied to each individual element and take into account the fields produced by every other radiating element. Unfortunately, a marginal increase in the desired accuracy of the coupling between elements requires a dramatic increase in required computational resources.

The consequences of designing an FSS structure using an inaccurate model can be costly. Often, actual FSS performance differs significantly from model predictions. This results

in a high percentage of expensive FSS structures that fail to meet specifications, driving

up the per-structure cost to the Air Force [Utt].


1.2  Research Goal


The purpose of this research is to determine the performance effects of perturbations of

the periodicity and dimensions of a frequency selective surface (FSS) using a reality-

based model.  Since current FSS analyses assume an infinite-by-infinite array of perfectly

placed and identically shaped elements, a more accurate model that takes into account

edge effects and material tolerances is desirable.  The Monte Carlo Method, an

approximation technique that is applied to mathematical problems [Fishman, p. 4] will be

utilized to give an overall sensitivity analysis of five design parameters (dipole length,

dipole placement in two directions, dielectric thickness, and dielectric material constant)

and how they interact with one another to affect FSS performance.  Six FSS performance

parameters will be studied:  main lobe peak, main lobe width, side lobe peak, side lobe

angle, ratio of side lobe peak to main lobe peak, and "low lobe" peak, where the "low

lobe" is defined as the first lobe encountered when scanning from an incident angle of

zero degrees to ninety degrees.  The effects of design parameter perturbations on these

FSS performance parameters will then be expressed in a general guide to show the

significant combinative effects of the design parameters.  Given a more complete

understanding of the interplay of the design parameters and their tolerances,

manufacturers should be able to better design FSS structures and dramatically lower the

per-FSS structure cost to the Air Force.

## 1.3 Assumptions

The model used in this research will be a dielectric slab covering an array of perfect, electrically-conducting (PEC) dipoles. It will be designed to operate as a bandstop filter at 15.29 GHz, which is typical of ground or satellite-based microwave communication systems. Variations in dielectric slab thickness are assumed to be uniform across the slab, and variations in dielectric material are likewise assumed to be uniform. Lastly, the dielectric slab surface is assumed to perfectly transmit incident electromagnetic fields; that is, no attenuation or scattering occurs due to the surface of the dielectric.

Due to the number of trials required by the Monte Carlo Method and the computational requirements of Method of Moments solution codes, the following FSS parameters are not considered in this model:

- Curved surfaces

- Multiple dielectric layers

- Multiple operating frequencies

- Surface roughness/impedance boundary condition

## 1.4 Scope

A short background of FSS design, including electromagnetic theory and analysis methods will be presented. Current models and the impacts of applying these models will be discussed, followed by a description of prior work in FSS perturbation analysis. A simple FSS model will then be designed, replicated repeatedly while introducing random tolerance errors, and the replications analyzed using the AIM (Adaptive Integral Method) code, developed by Boeing North American and Rockwell Science Center. The output will be statistically analyzed to show the sensitivity of FSS performance for given combinations of design parameters, and a set of prediction equations will be built using the results. The statistical analysis will reveal general trends of FSS performance based on the design parameters.

# 2 BACKGROUND

## 2.1 Overview

A basic understanding of the electromagnetic theory fundamental to frequency selective surfaces is necessary when performance and design are being studied. The Method of Moments and how it is applied in current models will be discussed, followed by the impacts of current models on FSS manufacturing. Finally, an overview of prior research in the area of analyzing perturbations in FSS analysis will be given.

## 2.2 FSS EM Theory

Standard electromagnetic theory can be applied to calculate the scattering from an arbitrary FSS. A basic example of this is the calculations involved with an array of slots in the x-z plane, infinitely long in both positive and negative x and z directions [Collins]. We excite the array with a plane wave at an arbitrary angle of incidence:
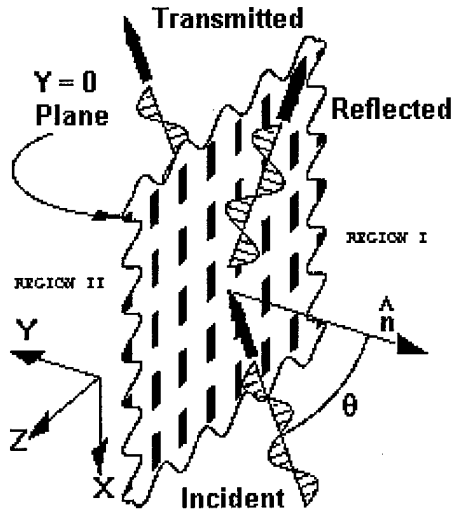
**Figure 2.1: Infinite-by-infinite dipole array**

We next enclose the FSS, assumed to be infinitely thin, with a Huygen surface. Using

Schelkunoff's surface equivalence theorem, we fill the "volume" with PEC and apply the

necessary impressed surface currents to satisfy our original boundary conditions. These

surface currents are:

$$\overline{J}_{eq} = \hat{n} \times \overline{H} \ , \tag{1.1}$$

$$\overline{M}_{eq} = \overline{E} \times \hat{n} \ , \tag{1.2}$$

where $\hat{n}$ is the outward normal from the Huygen surface, and $\overline{E}$ and $\overline{H}$ are the total

fields existing on the Huygen surface.

The Lorentz Reciprocity Theorem tells us that impressed electrical surface currents

cannot radiate from a PEC surface, so we must discard $J_{eq}$ and concentrate instead on the

impressed magnetic currents, $M_{eq}$.

7

We next note that the equivalent magnetic currents in Region I and Region II are equal and opposite to each other:

$$\overline{M}_I = -\overline{M}_{II} \tag{1.3}$$

This is due to the $\hat{n}$ vector switching signs between regions, and the continuity requirements for the electric fields across the PEC slots.

Now we enforce the boundary conditions of tangential H-field continuity across the slots, and form the following integral equation:

$$\overline{H}_{I,\tan}^{total}(\overline{R}) = \overline{H}_{II,\tan}^{total}(\overline{R}) \ , \tag{1.4}$$

where $\overline{H}_{I,\tan}^{total}(\overline{R})$ is the total tangential vector magnetic field in Region I, and

$\overline{H}_{II,\tan}^{total}(\overline{R})$ is the total tangential vector magnetic field in Region II.

In Region I, the total magnetic field can be separated into a generalized incident field solely caused by the incident plane wave, and a scattered field caused by the fields resulting from the magnetic currents on the slots:

$$\overline{H}_I^{total} = \overline{H}_I^{ginc} + \overline{H}_I^s \tag{1.5}$$

In Region II the total magnetic field is composed only of the field resulting from the magnetic current on the slots:

$$\overline{H}_{II}^{total} = \overline{H}_{II}^s \tag{1.6}$$

With some mathematical manipulation, we can use the continuity of the tangential fields and write the integral equation as follows:

$$\hat{n}_I \times \overline{H}_I^{ginc} = -\hat{n}_I \times \left[ \overline{H}_I^s(\overline{M}_I) + \overline{H}_{II}^s(\overline{M}_{II}) \right] \tag{1.7}$$

8

## 2.3 Method of Moments

Unfortunately, Equation (1.7) has no closed form solution. We thus apply the Method of Moments (MoM) to approximate the solution. This is done by assuming that the magnetic surface currents can be represented as a sum of N "basis functions." Ideally, these basis functions, $\Phi_n$, will be a close approximation to the true surface currents. Each basis function is multiplied by a unique "expansion coefficient," $V_n$, to give us the following magnetic current approximation:

$$\overline{M}_I^{approx} \cong \sum_{n=1}^{N} V_n \overline{\Phi}_n(\overline{R}')$$

(1.8)

We can now state that the true magnetic surface currents are equal to the approximate magnetic surface currents plus an error term:

$$\hat{n}_I \times \overline{H}_I^{ginc} = -\hat{n}_I \times \left[ \overline{H}_I^s (\sum V_n \overline{\Phi}_n) + \overline{H}_{II}^s (\sum V_n \overline{\Phi}_n) \right] + \overline{\varepsilon}(\overline{R}, V_1, ... V_n)$$

(1.9)

The vector error term is dependent upon both position and choice of the expansion coefficients. We want to eliminate the average weighted error by defining an inner product:

$$\langle \overline{f}, \overline{g} \rangle = \iint_{slot-areas} \overline{f}(\overline{R}) \cdot \overline{g}(\overline{R}) d\overline{R}$$

(1.10)

We choose N testing functions, $\Theta_m$ (R) defined over the slot areas, and define the test functions to be orthogonal to the error term:

$$\langle \overline{\varepsilon}, \overline{\Theta}_m \rangle = 0$$

(1.11)

9

Now we dot each term in Equation (1.9) by $\Theta_n$ and integrate over the slot areas:

$$\iint\limits_{slot-areas} \left[\hat{n}_I \times \overline{H}_I^{ginc}(\overline{R})\right] \cdot \overline{\Theta}_m(\overline{R})d\overline{R} \tag{1.12}$$

$$= -\iint\limits_{slot-areas} \left\{\hat{n}_I \times \left[\overline{H}_I^s(\sum V_n \overline{\Phi}_n) + \overline{H}_{II}^s(\sum V_n \overline{\Phi}_n)\right]\right\} \cdot \overline{\Theta}_m(\overline{R})d\overline{R}$$

Since $\overline{H}^s$ is the radiation integral--a linear operator--this is the equivalent of :

$$\iint\limits_{slot-areas} \left[\hat{n}_I \times \overline{H}_I^{ginc}(\overline{R})\right] \cdot \overline{\Theta}_m(\overline{R})d\overline{R} \tag{1.13}$$

$$= -\sum_{n=1}^{N} V_n \iint\limits_{slot-areas} \left\{\hat{n}_I \times \left[\overline{H}_I^s(\overline{\Phi}_n) + \overline{H}_{II}^s(\overline{\Phi}_n)\right]\right\} \cdot \overline{\Theta}_m(\overline{R})d\overline{R} \quad,$$

for all m, from 1 to N.

This yields a system of N equations:

$$\left[I_m\right] = \left[Y_{mn-I} + Y_{mn-II}\right]\left[V_n\right], \tag{1.14}$$

where $[I_m]$ is the "excitation vector," $[Y_{mn-I} + Y_{mn-II}]$ is the "coupling matrix," and $[V_n]$ is the "coefficient vector." This coefficient vector can then be solved for to obtain the expansion coefficients, giving us an approximation to the magnetic surface currents of the array.

## 2.4  Current FSS Models

A standard tool for FSS design that utilizes the Method of Moments to approximate the magnetic field integral equation (MFIE) is Henderson's Periodic Moment Method code (PMM) [Anderson].  The user inputs parameters which describe the basic geometry of the FSS, including element geometry, inter-element spacing, dielectric layer thickness and composition, etc.  PMM then models the FSS as an infinite-by-infinite array of identically shaped, perfectly placed elements, where each element is subject to the same coupling effects due to its surrounding elements. This infinite periodicity allows the application of Floquet's Theorem, which states that an incident plane wave will produce identical scattered fields from each element with an appropriate phase shift.  The result of this application is that the impressed surface currents must only be computed for a single element.  Floquet's theorem significantly reduces the computational burden of calculating the scattered fields, since the contribution of each element may be treated as equal in magnitude but with a phase shift introduced.

When Floquet's theorem cannot be applied, the computational resources (memory and CPU time) increase dramatically.  This is because each element will have its own unique scattering currents, and accordingly will couple with other elements uniquely.  This coupling must be handled by numerical analysis methods, most common of which is the Method of Moments.  Unfortunately, to increase the accuracy of the coupling matrix in method of moments computations we must add basis functions; an infinite number of basis functions would result in an infinitely accurate representation of the "true" surface

current impressed on each element. However, each basis function adds another dimension to the N-dimensional matrix computations and results in increasing the computational burden by $N^3$. Another significant increase in CPU requirements results from having to compute the surface currents of perhaps thousands of elements in a FSS, including the coupling between each of them.

2.5 Current Impacts

The consequences of designing an FSS structure using an inaccurate model can be costly. Manufacturers have often found that actual FSS performance differs significantly compared to predictions from models. This has forced manufacturers to try to manually "tweak" FSS structures into meeting specification standards; for example, sanding down the dielectric layer in certain areas may bring the FSS into compliance with the specifications. However, when this sanding technique is applied to another FSS of the same design, the technique may not work and the FSS may be discarded. This results in a high percentage of expensive FSS structures that fail to meet specification standards, driving up the per-structure cost to the Air Force [Utt]. When this per-structure cost is multiplied by the number of military systems that require FSS structures as part of a platform, the total cost to the government can increase significantly. System upgrades will also result in increased costs, since new FSS structures must be designed and manufactured.

## 2.6 Prior Research

The availability and power of CPU resources traditionally has limited research of FSS performance impacts. However, much work has been accomplished in the area of modeling FSS structures more realistically.

R. J. Luebbers and B. A. Munk studied the effects on FSS performance that occurred when dielectric layers were placed on top and bottom of a standard FSS model, which was an infinite-by-infinite array of slots in a PEC plane [Luebbers]. Modal analysis solutions were developed for the fields produced by the FSS, and FSS performance was able to be controlled by the manipulation of the dielectric parameters. The model used in this research was closer to a real, manufacturable FSS structure since it wasn't based on an array floating in free space. However, it was still idealized since it assumed an infinite-by-infinite array of ideally shaped and placed elements.

A comparison of CPU requirements for analyzing FSS structures demonstrated the utility of mathematical approximations in FSS analysis [Koleck]. A small-size, finite FSS was first analyzed using the Method of Moments, and the large increase in CPU resources required by a relatively small increase in finite FSS size was shown. The FSS was then analyzed using a plane wave spectral decomposition approach, which was made possible by treating the FSS as an infinite-by-infinite array. This reduced CPU requirements significantly, but resulted in the analysis of a model with unrealistic design parameters.

J. Paul Skinner addressed the problem of CPU limitations in his PhD dissertation [Skinner], where he derived the field calculations for a finite-by-infinite array model. He also developed a FORTRAN code that could analyze FSS structures using his finite-by-infinite model. This reduced the required CPU resources significantly, and was a more realistic model than the standard infinite-by-infinite model.

Edwin Chavez's master's thesis [Chavez] took Skinner's model and altered the FORTRAN code to introduce random perturbations in the dipole length, dipole placement, and column spacing. He altered the standard deviation of the single parameters of dipole length, dipole width, and dipole column spacing in the finite direction, and observed the impact on main lobe peak. Although this work used a more realistic, infinite-by-finite model with material tolerances factored in, it did not address the combinative effects of different design parameters on FSS performance.

Roger A. Hill and B. A. Munk introduced perturbations in element dimension and element placement into a single layer, dual band FSS model [Hill]. The results were used to establish guidelines for dual-band FSS design that would prevent anomalous performance behaviors from occurring at the two design frequencies. The guidelines were successfully used to design a dual-band FSS with a large-small element design. However, the guidelines were applied with unsuccessful results to two other FSS designs, one using a composite element and one using a different large-small element design.

In James Godsey's PhD dissertation [Godsey], the effects of adding width and spacing perturbations to a two-dimensional strip grating were studied. The center elements were assumed to have identical impressed surface currents, which enabled Floquet's theorem to be partially applied. The edges of the FSS were treated with the Born approximation, in which the unknown scattered fields are replaced by the incident fields. A statistical average power pattern was then calculated based on the radiated fields and compared to the power pattern produced by that of a strip grating with ideal dimensions.

## 2.7 Summary

Electromagnetic theory governing the behavior of frequency selective surfaces has resulted in the necessary application of numerical analysis methods such as the Method of Moments. These analysis methods require increasing computational resources for increasingly accurate solutions, which has resulted in the formulation of FSS models that incorporate assumptions that alleviate the CPU burden. While these models are favorable in terms of computational efficiency, they may diverge from realistic design considerations.

A study of tolerances in a reality-based FSS model is required to show the impacts of real design tolerances and finite dimension effects on FSS performance. The performance impacts of specific FSS design parameters could then be quantified, giving FSS manufacturers a more complete understanding of which parameter tolerances are most important. This study and the results are given in the following chapters.

# 3 METHODOLOGY

## 3.1 Overview

A reality-based model is now constructed, with the goal of relating six output performance parameters to five input design parameters. This will be achieved by implementing a full-factorial experimental design, where 32 configurations of input performance parameters will be developed. Using the Monte Carlo method, normally distributed random errors will be introduced into the input performance parameters, with variances determined by the experimental design. For each configuration, 25 unique FSS model replications will be generated, and subsequently analyzed using the AIM code.

## 3.2 Model Description

This research studies the impacts of the variation of five parameters on the performance of a dipole array covered by a rectangular dielectric slab. Performance will be measured in terms of six performance parameters:

1. Main lobe peak

2. Main lobe width

3. Side lobe peak

4. Side lobe location

5. Side lobe / Main lobe ratio

6. Low lobe peak

The low lobe peak is defined here as the peak of the first lobe as incident angle is varied from zero degrees to ninety degrees.

It has been shown that variance of dipole width has virtually no impact on FSS performance [Chavez, p. 3-24], and thus this parameter is not studied. The five design parameters we will examine are:

1. Dipole length (x-directed)
2. Dipole placement in the x-direction
3. Dipole placement in the z-direction
4. Dielectric thickness
5. Complex dielectric constant

The frequency selective surface is patterned after one designed by E.V. Chavez [Chavez, p. 3-2], but adapted to perform at 15.29 GHz instead of 10 GHz. It consists of a 20 x 20 array of x-directed PEC dipoles contained in the x-z plane, covered by a single dielectric layer. Figure 3.1 is a 2 x 2 version of the model that shows the FSS design parameters. The FSS has the following parameters:

1. Dipole dimension in x-direction (length, Lx): 1.0 cm
2. Dipole dimension in z-direction (width, Lz): 0.1 cm

3. Dipole spacing in x-direction (Dx): 1.447 cm

4. Dipole spacing in z-direction (Dz): 0.863 cm

5. Slab thickness (t): 1.0 cm

6. Slab dielectric constant (epsilon): 2.55

7. Operating Frequency: 15.29 GHz
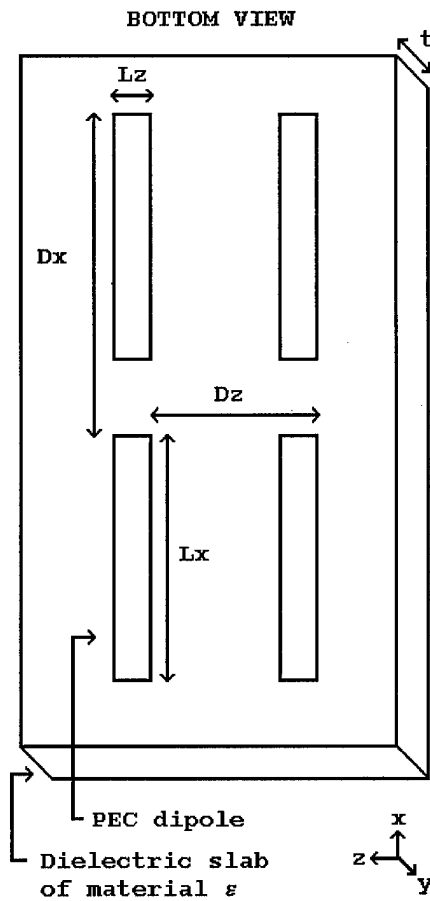


**Figure 3.1: FSS Design Parameter Geometry**

The incident electric field is normalized to 1 V/M and is TMz polarized, to agree with the

FSS dipole orientation. A frequency sweep of the model using PMM is shown below.
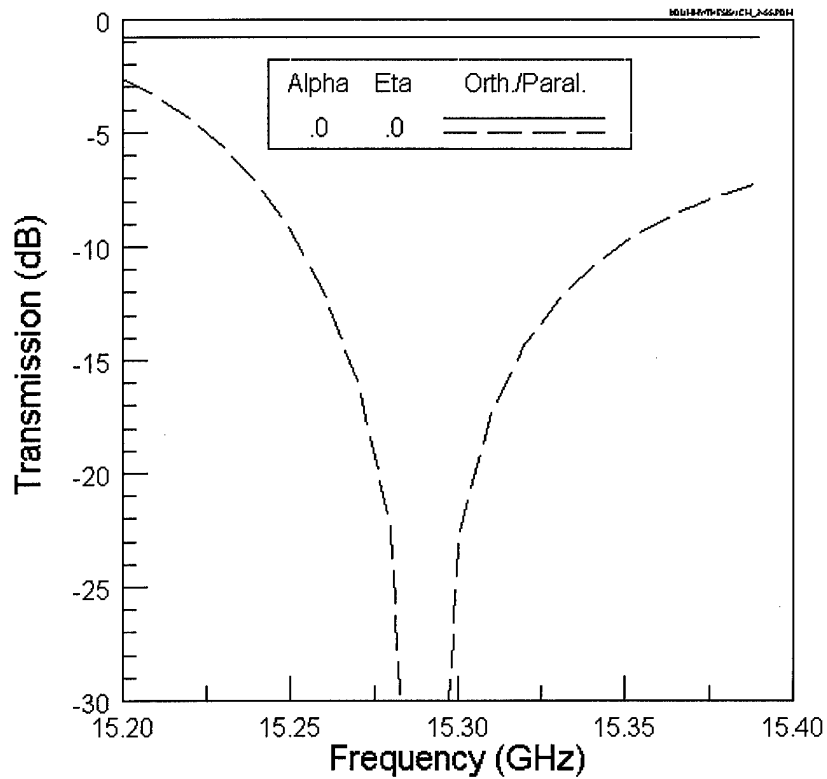
**Figure 3.2: Frequency sweep of model using PMM**

## 3.3 Experiment Design

Each parameter is measured at two levels: a "low" tolerance and a "high" tolerance.

Using a full-factorial experimental design approach, this results in $2^5$, or 32

configurations [Montgomery, p. 181]. Figure 3.1 shows the test matrix, containing the

tolerance for each configuration. The notation "$\sigma_x$" denotes the value in the table as one

standard deviation away from the mean, or "ideal" value of the performance parameter

19

"x." These numbers were assigned the listed values to ensure measurable performance impacts would occur, and resulted from the data of preliminary test runs.

| CONFIGURATION | $\sigma_{Lx}$ (cm) | $\sigma_{Dx}$ (cm) | $\sigma_{Dz}$ (cm) | $\sigma_t$ (cm) | $\sigma_\varepsilon$ |
|---|---|---|---|---|---|
| 1 | 0.01 | 0.01 | 0.01 | 0.01 | 0.01 |
| 2 | 0.1 | 0.01 | 0.01 | 0.01 | 0.01 |
| 3 | 0.01 | 0.05 | 0.01 | 0.01 | 0.01 |
| 4 | 0.01 | 0.01 | 0.03 | 0.01 | 0.01 |
| 5 | 0.01 | 0.01 | 0.01 | 0.03 | 0.01 |
| 6 | 0.01 | 0.01 | 0.01 | 0.01 | 0.03 |
| 7 | 0.1 | 0.05 | 0.01 | 0.01 | 0.01 |
| 8 | 0.1 | 0.01 | 0.03 | 0.01 | 0.01 |
| 9 | 0.1 | 0.01 | 0.01 | 0.03 | 0.01 |
| 10 | 0.1 | 0.01 | 0.01 | 0.01 | 0.03 |
| 11 | 0.01 | 0.05 | 0.03 | 0.01 | 0.01 |
| 12 | 0.01 | 0.05 | 0.01 | 0.03 | 0.01 |
| 13 | 0.01 | 0.05 | 0.01 | 0.01 | 0.03 |
| 14 | 0.01 | 0.01 | 0.03 | 0.03 | 0.01 |
| 15 | 0.01 | 0.01 | 0.03 | 0.01 | 0.03 |
| 16 | 0.01 | 0.01 | 0.01 | 0.03 | 0.03 |
| 17 | 0.1 | 0.05 | 0.03 | 0.03 | 0.03 |
| 18 | 0.01 | 0.05 | 0.03 | 0.03 | 0.03 |
| 19 | 0.1 | 0.01 | 0.03 | 0.03 | 0.03 |
| 20 | 0.1 | 0.05 | 0.01 | 0.03 | 0.03 |
| 21 | 0.1 | 0.05 | 0.03 | 0.01 | 0.03 |
| 22 | 0.1 | 0.05 | 0.03 | 0.03 | 0.01 |
| 23 | 0.01 | 0.01 | 0.03 | 0.03 | 0.03 |
| 24 | 0.01 | 0.05 | 0.01 | 0.03 | 0.03 |
| 25 | 0.01 | 0.05 | 0.03 | 0.01 | 0.03 |
| 26 | 0.01 | 0.05 | 0.03 | 0.03 | 0.01 |
| 27 | 0.1 | 0.01 | 0.01 | 0.03 | 0.03 |
| 28 | 0.1 | 0.01 | 0.03 | 0.01 | 0.03 |
| 29 | 0.1 | 0.01 | 0.03 | 0.03 | 0.01 |
| 30 | 0.1 | 0.05 | 0.01 | 0.01 | 0.03 |
| 31 | 0.1 | 0.05 | 0.01 | 0.03 | 0.01 |
| 32 | 0.1 | 0.05 | 0.03 | 0.01 | 0.01 |

**Figure 3.3:  Test matrix**

## 3.4  Monte Carlo Method

The Monte Carlo Method is an approximation technique that is applied to mathematical problems, ranging from investment-payoff models to particle transport predictions in nuclear systems [Brown, p. 4]. The method involves "rolling the dice" to pick points within a bounded sample space (hence, the name "Monte Carlo") and observing the outcome to estimate a solution space.

For each configuration, twenty-five different geometric input files are generated. The geometry of each input file is created such that each parameter is varied with a normal distribution, centered on the ideal value within one standard deviation of the tolerance value. For example, in some configurations a dipole with an ideal length of 1.0 cm is perturbed using a tolerance of 0.05 cm, so that the final length is 1.0 cm +/- 0.05 cm with a confidence level of approximately 68.8 %. This process is repeated for every dipole in the array, resulting in a 20 x 20 array of dipoles with lengths being distributed normally around a mean of 1.0 cm, with a standard deviation of 0.05 cm.

A histogram of the values of the design parameters should follow the standard normal distribution function [Taylor, p. 112]:

$$f_{X,\sigma}(x) = \frac{1}{\sigma\sqrt{2\pi}} \exp\left(\frac{-(x-X)^2}{2\sigma^2}\right), \qquad (3.4)$$

where X is the mean, x is the measured value, and $\sigma$ is the standard deviation.

To utilize this formula in a computer code that will produce geometric input files with normally distributed dimensions, it must be transformed to give an algorithm that requires two uniform random numbers, $x_1$ and $x_2$, to produce a normal random number [Press, p. 216-217]. Given arbitrary values for the mean and standard deviation, the formula for normal random numbers, $y_{1,2}^{norm}$, is as follows:

$$y_{1,2}^{norm} = \bar{x} + \left[ \sigma \cdot x_{1,2} \cdot \sqrt{\frac{-2 \log(x_1^2 + x_2^2)}{x_1^2 + x_2^2}} \right], \tag{3.5}$$

where $\bar{x}$ is the mean and $\sigma$ is the standard deviation. This algorithm is chosen for its computational efficiency, since it requires a few simple arithmetic computations to generate two normal random numbers. Every time a random number is generated within the code, it is written to a data file to ensure a normal distribution. This distribution is shown in the figure below.
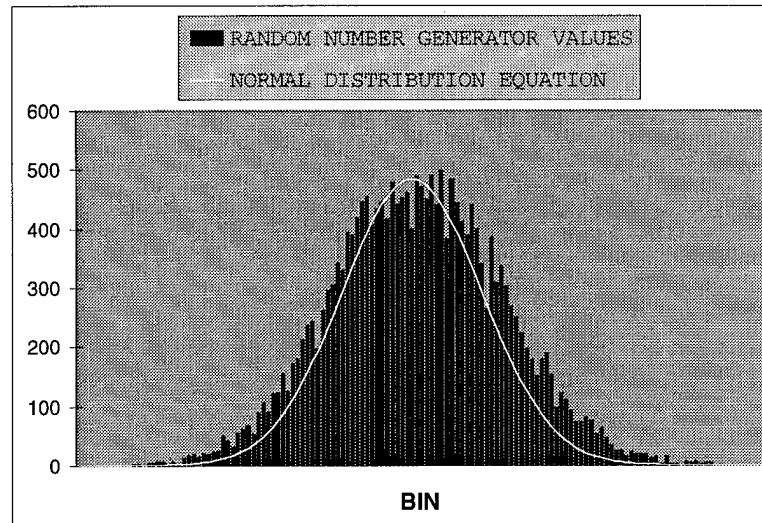
**Figure 3.4: Random Number Generator Plot**

3.5 Implementation

Due to the large number of runs required in this research, the SGI Origin 2000 machine at

the ASC Major Shared Resource Center (MSRC) located at Wright-Patterson AFB, OH

is used to run the Method of Moments code. All technical details such as batch job

submission, script format, and notes regarding MSRC usage are included in Appendix C.

A computer code using the flowchart structure shown in the figure below is written in

C++ to produce the acad input files with variable tolerances, employing the normal

random number generating algorithm described above. Using this code, 25 files for each

of the 32 configurations are created, a total of 800 acad input files. The same code also

creates the 800 region input files and the 800 global input files that the AIM code

requires to run. Geometric similarities allow a single patch input file and a single

material input file. In all, a total of 2402 unique input files are generated for this research. The AIM file formats are described in detail in Appendix B.
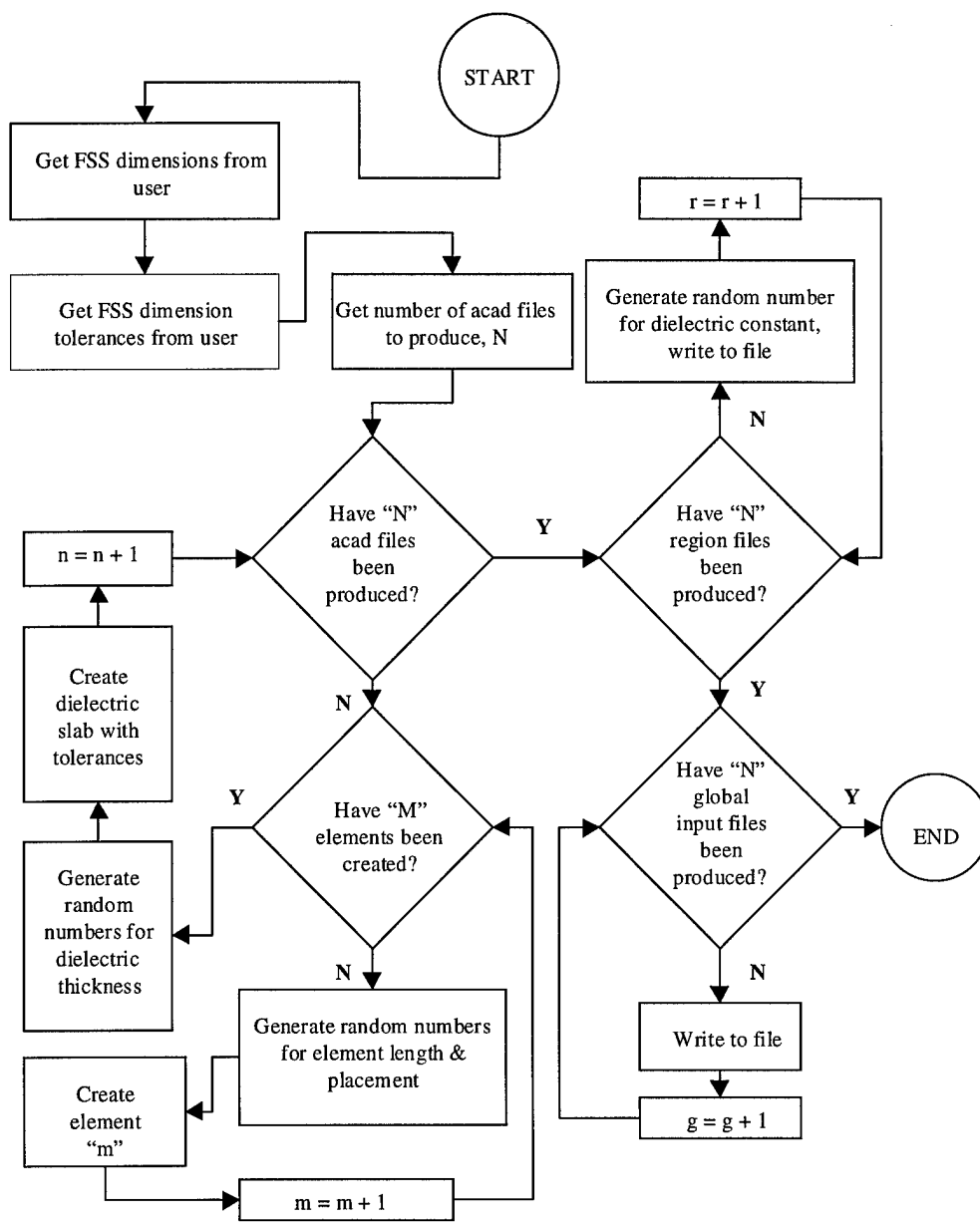


**Figure 3.5: Input file generation flowchart**

## 3.6 Data Extraction

Once the output files are obtained, a Microsoft Excel 7.0 macro [Hendrix] is applied to each configuration to extract the performance parameters for each of the 25 input files. These performance parameters (main lobe peak, main lobe width, first side lobe peak and location, side lobe peak/main lobe peak ratio, and low lobe peak) are exported into a columnar file format, able to be read by a statistical analysis software utility called JMP.

## 3.7 Empirical Model Construction

After the Monte Carlo Method is performed on each of the 32 configurations, the results are analyzed to find the relationship between the five design parameters and the six performance parameters studied. JMP is utilized to perform the rigorous statistical analysis required to determine the impacts of the five parameters on the FSS performance. An empirical model is then constructed, giving us a quadratic-order predictive model that shows the impacts of the different combinations of FSS parameters.

## 3.8 AIM Description

The FSS models with tolerances added are analyzed using a computational electromagnetic code called the AIM (Adaptive Integral Method) code, developed by Boeing North American and Rockwell Science Center. This code is an iterative, fast integral equation solver that computes radar signatures of arbitrarily shaped three-dimensional objects.

AIM utilizes two sets of basis functions for computing impedance matrices, one for the near-field and one for the far-field. The physical equivalent of using these sets of basis functions is the replacement of the original current distribution with an approximately equivalent set of point-like sources, located at regularly spaced nodes in Cartesian coordinates. These point-like sources produce far-field measurements nearly identical to the original current distribution. To ensure agreement with the Method of Moments solution, the impedance matrices are compared and, if the required tolerance is not achieved, the grid spacing between nodes is reduced until the tolerance criteria is met. AIM then computes the far-field by using the Fast Fourier Transform (FFT), which produces a Toeplitz impedance matrix instead of the familiar "dense" impedance matrix resulting from the Method of Moments [Bleszynski, Section 6.3].

This Toeplitz matrix is much more compact than the dense impedance matrix in Method of Moments solutions, resulting in memory requirements of $O(N^\alpha)$, where $\alpha \leq 1.5$ and N is the number of unknowns. In contrast, Method of Moments solvers require $O(N^3)$ in memory for full matrix solutions, and $O(N^2)$ in memory for iterative matrix solutions. Similarly, the AIM Toeplitz matrix algebraic operation count per iteration is $O(N^\alpha \log N)$, while the Method of Moments iterative solvers require $O(N^2)$ counts per iteration, respectively [Bleszynski, section 1.1].

## 3.9 Summary

A simple, realistic FSS model is constructed for analyzing the impact on performance of design parameter tolerances. A full-factorial experimental design is utilized to determine the combinative effects of the design parameters on FSS performance, resulting in 32 different configurations of design parameter tolerances. Applying the Monte Carlo method, the model is replicated 25 times for each configuration, and normal random errors are introduced into the design parameters. Each replication is analyzed using the AIM code, and a sensitivity analysis is performed using the JMP utility to determine trends in performance effects.

# 4  RESULTS/ANALYSIS

## 4.1  Overview

Representative data plots produced by the AIM code are given in the following section,

and general trends in performance output are discussed.  A performance parameter

impact analysis is performed, and a comprehensive table of performance impacts is

given.

## 4.2  Representative Data Plots

The following section contains representative plots of data collected for this research and

used in the statistical analysis.  A representative pattern plot and scatter plot are given.

All plots are included in Appendix A, Data Plots and Tables.

### 4.2.1  Representative Pattern Plot

Figure 4.1 shows a representative pattern plot of configuration 1 (all parameters at a high

tolerance), configuration 16 (dipole length and placement in two directions at a high

tolerance, dielectric thickness and material constant at a low tolerance), and configuration

17 (all parameters at a low tolerance).  Note the general degradation of the pattern as the

tolerances of the performance parameters is lowered.
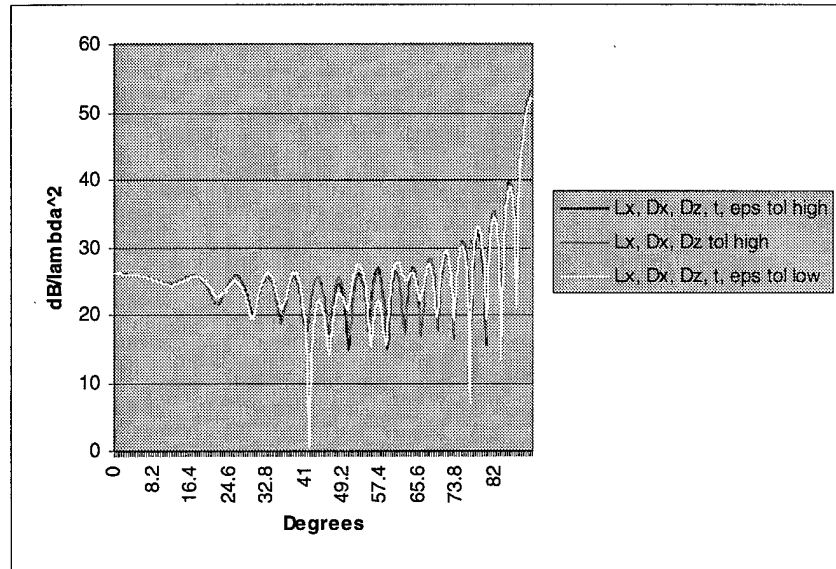
**Figure 4.1: Representative Pattern Plot**

The pattern plots show the change in performance parameters as the design parameter tolerances are varied. These performance parameters were then extracted into a single data file.

4.2.2 Representative Scatter Plot

A representative scatter plot of the data for a single performance parameter, main lobe peak, is shown in Figure 4.2. The scatter plot shows all data points plotted versus the independent variable, with random noise introduced in the x-direction to help identify trends.

Once again, all scatter plots are given in Appendix A, Data Plots and Tables.

29
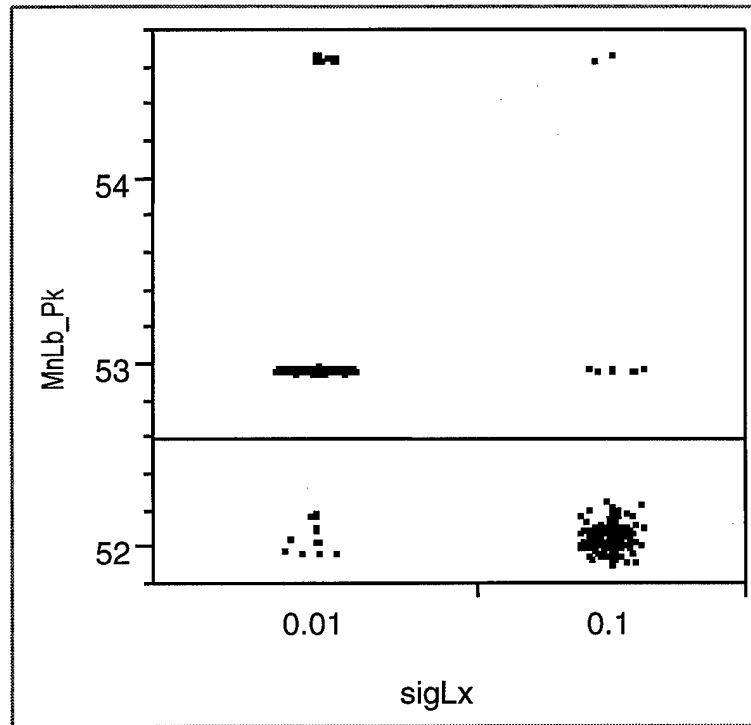
**Figure 4.2: Main lobe peak by variation in dipole length**

As a rule, the values for the performance parameters spread out when a lower tolerance is applied. A description of the effects of each design parameter on each performance parameter follows.

1. Main lobe peak

Lowering the tolerance of dipole length yielded lower values for the main lobe peak, and had the effect of distributing the data over a wider range. This is reasonable, since the number of dipoles with a length equal to a half of a wavelength will be decreased when a lower tolerance is applied.

## 2. Main lobe width

The main lobe width increased when tolerances of dipole placement in the "width" direction, dielectric thickness, and dielectric constant were each lowered. This decrease in performance could be due to the increased coupling effects caused by dipole shifts in the dipole "width" direction, which are much stronger than coupling in dipole "length" direction. This is because the familiar "donut" antenna pattern for a radiating dipole results in a stronger coupling between dipoles placed side by side, as compared to dipoles placed end to end.

Since one benefit of placing dielectric layers over FSS structures is a decrease in main lobe width, we can understand that decreasing the tolerances of dielectric thickness and dielectric material composition would also give a corresponding increase in main lobe width.

## 3. Side lobe peak

Values for the side lobe peak were distributed over a wider range when dipole length tolerance was lowered. This was similar to the effect observed for the main lobe peak.

## 4. Side lobe angle

The side lobe angle, which is the angular location of the side lobe peak, decreased when each of the five design parameter tolerances were lowered. This indicates a broadening of lobes, which is another mark of performance degradation.

5. Side lobe / main lobe ratio

The values of the ratio of the side lobe peak to the main lobe went from a tight cluster to a wide, scattered distribution when dipole length tolerance was lowered. Clearly, this performance parameter is directly related to the main lobe peak and side lobe peak parameters.

6. Low lobe peak

As tolerances for dipole length were lowered, values for the low lobe peak became scattered and more widely distributed. This trend was similar to the trends in the main lobe peak, side lobe peak, and side/main lobe ratio performance parameters.

4.3 Performance Parameter Impact Analysis

The JMP utility was used to determine the performance impact effects of the design parameters, using a standard least squares model. Before we proceed with the analysis, several statistical terms must be defined.

"Least squares means" are the statistics that are compared when effects on output are tested. They are the predicted values for the response across the levels of some parameter, given that all the other parameters in the model are held at some "neutral" value. They may not reflect typical real-world values of the response if the values that the factors are set to do not reflect prevalent combinations of values in the real world. They are mainly used for the purpose of comparison in experimental situations.

"F Ratio" is the statistic for testing that the effect on an output parameter is zero. It is formed as the ratio of the mean square for the parameter divided by the mean square for error. The mean square for the parameter is the sum of squares for the parameter divided by its degrees of freedom. In situations where a subsequent term is specified to be an error term, the mean square for this error term is used instead of mean square for error as the denominator of the F Ratio. This specification is used in split-plot and repeated-measure models where there are different observational units for different layers of the model.

The term "Prob > F" is the observed significance probability for the F Ratio. It is the probability that, given that the hypothesis is true, that a larger F statistic would occur due to random error. Statistical convention states that a probability less than 0.05 is considered a statistically significant effect; that is, there is a 95% probability that the effect is due to a given parameter [SAS Institute].

### 4.3.1 Representative Performance Parameter Sensitivity Analysis

The following figure shows the performance parameter sensitivity analysis for one

performance parameter, main lobe peak.

Response: MnLb_Pk

Summary of Fit

| | |
|---|---|
| RSquare | 0.802144 |
| RSquare Adj | 0.793111 |
| Root Mean Square Error | 0.247779 |
| Mean of Response | 52.60545 |

Effect Test

| Source | Nparm | DF | Sum of Squares | F Ratio | Prob>F |
|---|---|---|---|---|---|
| sigLx | 1 | 1 | 141.15052 | 2299.083 | <.0001 |
| sigDx | 1 | 1 | 0.00991 | 0.1614 | 0.6880 |
| sigLx*sigDx | 1 | 1 | 0.57018 | 9.2872 | 0.0024 |
| sigDz | 1 | 1 | 2.10417 | 34.2731 | <.0001 |
| sigLx*sigDz | 1 | 1 | 0.34878 | 5.6809 | 0.0174 |
| sigDx*sigDz | 1 | 1 | 0.33164 | 5.4018 | 0.0204 |
| sigLx*sigDx*sigDz | 1 | 1 | 2.22206 | 36.1933 | <.0001 |
| sigt | 1 | 1 | 0.61178 | 9.9648 | 0.0017 |
| sigLx*sigt | 1 | 1 | 0.04951 | 0.8064 | 0.3695 |
| sigDx*sigt | 1 | 1 | 0.02735 | 0.4456 | 0.5047 |
| sigLx*sigDx*sigt | 1 | 1 | 0.53578 | 8.7269 | 0.0032 |
| sigDz*sigt | 1 | 1 | 2.20416 | 35.9017 | <.0001 |
| sigLx*sigDz*sigt | 1 | 1 | 0.35965 | 5.8580 | 0.0158 |
| sigDx*sigDz*sigt | 1 | 1 | 0.37539 | 6.1144 | 0.0137 |
| sigLx*sigDx*sigDz*sigt | 1 | 1 | 2.08196 | 33.9114 | <.0001 |
| sigeps | 1 | 1 | 0.54322 | 8.8480 | 0.0030 |
| sigLx*sigeps | 1 | 1 | 0.02747 | 0.4474 | 0.5038 |
| sigDx*sigeps | 1 | 1 | 0.01653 | 0.2693 | 0.6040 |
| sigLx*sigDx*sigeps | 1 | 1 | 0.49231 | 8.0188 | 0.0048 |
| sigDz*sigeps | 1 | 1 | 2.14518 | 34.9411 | <.0001 |
| sigLx*sigDz*sigeps | 1 | 1 | 0.35701 | 5.8150 | 0.0162 |
| sigDx*sigDz*sigeps | 1 | 1 | 0.31826 | 5.1839 | 0.0231 |
| sigLx*sigDx*sigDz*sigeps | 1 | 1 | 2.25498 | 36.7296 | <.0001 |
| sigt*sigeps | 1 | 1 | 0.48582 | 7.9131 | 0.0050 |
| sigLx*sigt*sigeps | 1 | 1 | 0.01592 | 0.2594 | 0.6107 |
| sigDx*sigt*sigeps | 1 | 1 | 0.04963 | 0.8084 | 0.3689 |
| sigLx*sigDx*sigt*sigeps | 1 | 1 | 0.60355 | 9.8307 | 0.0018 |
| sigDz*sigt*sigeps | 1 | 1 | 2.17370 | 35.4057 | <.0001 |
| sigLx*sigDz*sigt*sigeps | 1 | 1 | 0.35444 | 5.7731 | 0.0165 |
| sigDx*sigDz*sigt*sigeps | 1 | 1 | 0.30072 | 4.8982 | 0.0272 |
| sigLx*sigDx*sigDz*sigt*sigeps | 1 | 1 | 2.29179 | 37.3291 | <.0001 |

**Figure 4.3: Parameter Impact Analysis Table--Main Lobe Peak**

34

The parameter impact analysis tables for each performance parameter are given in

Appendix A, Data Plots and Tables.


4.3.2  Performance Parameter Impact Table


The design parameter combinations that affected each performance parameter with a 95%

confidence level or higher are shown in Figure 4.4, Parameter Impact Summary Table.

Combinations with a 95% confidence level are marked with a small "x," and

combinations having a confidence level of 99.99% are marked with a large"X."

| DESIGN PARAMETER COMBINATION | PERFORMANCE IMPACT | | | | | |
|---|---|---|---|---|---|---|
| | MAIN LOBE PEAK | MAIN LOBE WIDTH | SIDE LOBE PEAK | SIDE LOBE ANGLE | SIDE/MAIN LOBE RATIO | LOW LOBE PEAK |
| $\sigma_{Lx}$ | **X** | **X** | **X** | x | **X** | x |
| $\sigma_{Dx}$ | | x | | | | x |
| $\sigma_{Lx} \times \sigma_{Dx}$ | x | x | x | x | x | x |
| $\sigma_{Dz}$ | **X** | | x | x | | **X** |
| $\sigma_{Lx} \times \sigma_{Dz}$ | x | x | x | x | | x |
| $\sigma_{Dx} \times \sigma_{Dz}$ | x | **X** | | **X** | | |
| $\sigma_{Lx} \times \sigma_{Dx} \times \sigma_{Dz}$ | **X** | | x | x | | **X** |
| $\sigma_{t}$ | x | x | | **X** | | x |
| $\sigma_{Lx} \times \sigma_{t}$ | | x | | x | | x |
| $\sigma_{Dx} \times \sigma_{t}$ | | x | | x | | x |
| $\sigma_{Lx} \times \sigma_{Dx} \times \sigma_{t}$ | x | | x | **X** | | x |
| $\sigma_{Dz} \times \sigma_{t}$ | **X** | x | x | x | | x |
| $\sigma_{Lx} \times \sigma_{Dz} \times \sigma_{t}$ | x | | | | | x |
| $\sigma_{Dx} \times \sigma_{Dz} \times \sigma_{t}$ | x | x | | | | x |
| $\sigma_{Lx} \times \sigma_{Dx} \times \sigma_{Dz} \times \sigma_{t}$ | **X** | | x | | | x |
| $\sigma_{\varepsilon}$ | x | x | x | x | x | x |
| $\sigma_{Lx} \times \sigma_{\varepsilon}$ | | x | | **X** | | x |
| $\sigma_{Dx} \times \sigma_{\varepsilon}$ | | **X** | | x | | x |
| $\sigma_{Lx} \times \sigma_{Dx} \times \sigma_{\varepsilon}$ | x | | | **X** | | **X** |
| $\sigma_{Dz} \times \sigma_{\varepsilon}$ | **X** | | | x | | **X** |
| $\sigma_{Lx} \times \sigma_{Dz} \times \sigma_{\varepsilon}$ | x | x | x | | | x |
| $\sigma_{Dx} \times \sigma_{Dz} \times \sigma_{\varepsilon}$ | x | x | | x | | x |
| $\sigma_{Lx} \times \sigma_{Dx} \times \sigma_{Dz} \times \sigma_{\varepsilon}$ | **X** | | **X** | | x | x |
| $\sigma_{t} \times \sigma_{\varepsilon}$ | x | x | x | | x | x |
| $\sigma_{Lx} \times \sigma_{t} \times \sigma_{\varepsilon}$ | | | | | | x |
| $\sigma_{Dx} \times \sigma_{t} \times \sigma_{\varepsilon}$ | | x | | | | |
| $\sigma_{Lx} \times \sigma_{Dx} \times \sigma_{t} \times \sigma_{\varepsilon}$ | x | | | x | | **X** |
| $\sigma_{Dz} \times \sigma_{t} \times \sigma_{\varepsilon}$ | **X** | | x | **X** | | x |
| $\sigma_{Lx} \times \sigma_{Dz} \times \sigma_{t} \times \sigma_{\varepsilon}$ | x | x | | x | | x |
| $\sigma_{Dx} \times \sigma_{Dz} \times \sigma_{t} \times \sigma_{\varepsilon}$ | x | | | **X** | | x |
| $\sigma_{Lx} \times \sigma_{Dx} \times \sigma_{Dz} \times \sigma_{t} \times \sigma_{\varepsilon}$ | **X** | x | x | x | | x |

**Figure 4.4: Parameter Impact Summary Table**

From the summary table, it is clear that the most statistically significant effect on all performance parameters was given by lowering the tolerance of dipole length. In addition to affecting all six parameters with a minimum confidence level of 95% of a statistical effect, it was the only combination of design parameters (in this case, a single design parameter) that had a 99.99% confidence level of a statistical effect on four of six performance parameters.

### 4.3.3 Performance Parameter Summary Equation

The ratio of the side lobe peak to the main lobe peak is an indication of the efficiency of the FSS structure in terms of power. Ideally, the power within the main lobe should be much greater in magnitude than the power within the side lobe, as measured at the peaks. Therefore, a predictive equation governing this ratio would be helpful in determining which design parameters are most influential on FSS efficiency. This was accomplished through a linear regression analysis [Green, p. 140].

We first defined a new variable, $x_p$, defined by taking the high tolerance value, $\sigma_p^{high}$, and the low tolerance value, $\sigma_p^{low}$, for a parameter "p" and transforming them into 1 and -1, respectively. This results in a linear equation:

$$x_p = \frac{\sigma_p - \dfrac{\sigma_p^{high} + \sigma_p^{low}}{2}}{\dfrac{\sigma_p^{high} - \sigma_p^{low}}{2}} \tag{4.1}$$

Using the above transformation, we performed a regression analysis to obtain a predictive equation governing the behavior of side to main lobe peak ratio. Using the impacts taken from the Performance Impact Summary Table that have a 99.99% confidence level, the predictive equation will have the following form:

$$R = a_0 + a_{Lx} x_{Lx} + a_{LxDx} x_{Lx} x_{Dx} + a_{Eps} x_{Eps} + a_{LxDxDzEps} x_{Lx} x_{Dx} x_{Dz} x_{Eps} \quad (4.2)$$
$$+ a_{tEps} x_t x_{Eps} + \varepsilon$$

where R is the side to main lobe peak ratio, $a_0$ is the intercept, $a_p$ is the coefficient for the specific parameter combination, and $\varepsilon$ is the error.

We next perform a linear regression analysis to obtain the coefficients for Equation (4.2). The results of the analysis are shown below:

Regression Model for Side/Main Lobe Ratio

Response: Sd/Mn Ratio

Summary of Fit

| | |
|---|---|
| RSquare | 0.101671 |
| RSquare Adj | 0.0953 |
| Root Mean Square Error | 0.00745 |
| Mean of Response | 0.749561 |

Parameter Estimates

| Term | Estimate | Std Error | t Ratio | Prob>ltl |
|---|---|---|---|---|
| Intercept | 0.7493388 | 0.000281 | 2664.8 | 0.0000 |
| x_Lx | -0.002105 | 0.000281 | -7.49 | <.0001 |
| x_Lx*Dx | 0.0007825 | 0.00028 | 2.80 | 0.0053 |
| x_eps | -0.000585 | 0.00028 | -2.09 | 0.0366 |
| x_Lx*Dx*Dz*eps | -0.00069 | 0.00028 | -2.46 | 0.0140 |
| x_t*eps | 0.0006404 | 0.00028 | 2.29 | 0.0223 |

Effect Test

| Source | Nparm | DF | Sum of Squares | F Ratio | Prob>F |
|---|---|---|---|---|---|
| x_Lx | 1 | 1 | 0.00311075 | 56.0438 | <.0001 |
| x_Lx*Dx | 1 | 1 | 0.00043377 | 7.8148 | 0.0053 |
| x_eps | 1 | 1 | 0.00024343 | 4.3857 | 0.0366 |
| x_Lx*Dx*Dz*eps | 1 | 1 | 0.00033692 | 6.0701 | 0.0140 |
| x_t*eps | 1 | 1 | 0.00029112 | 5.2449 | 0.0223 |

**Figure 4.5: Linear Regression Analysis Table**

Incorporating the coefficients given above into Equation (4.2), we get:

$$R = \left(7.493 \times 10^{-1}\right) + \left(-2.105 \times 10^{-3}\right)x_{Lx} + \left(7.825 \times 10^{-4}\right)x_{Lx}x_{Dx}$$
$$+ \left(-5.850 \times 10^{-4}\right)x_{Eps} + \left(-6.900 \times 10^{-4}\right)x_{Lx}x_{Dx}x_{Dz}x_{Eps}$$
$$+ \left(6.404 \times 10^{-4}\right)x_t x_{Eps} + \varepsilon$$

(4.3)

Equation (4.3) shows that the design parameters having the most significant effect on the side to main lobe peak ratio are dipole length and dielectric material constant.

## 4.4 Summary

The performance parameter data showed clear, statistically significant trends as design parameter tolerance was varied. This data was analyzed using a standard least squares model platform, and the relation of the effects of the combinations of design parameters to performance parameters was quantified and displayed in a summary table. A linear regression analysis was performed to determine design parameter effects on the ratio of the side lobe peak to the main lobe peak, and a predictive equation was formed using the results.

# 5 CONCLUSIONS/RECOMMENDATIONS

## 5.1 Conclusions

The Monte Carlo Method provided a simple foundation upon which to build a predictive model of FSS performance, using a standard least squares model. Six FSS performance parameters were studied, and the effects of combinations of the six design parameters were discussed and quantified.

The most significant design parameter that affected performance was dipole length. In addition to affecting all six performance outputs, the effects themselves were the most statistically stringent of any other input parameter or combination.

Two other specific combinations that affected all six parameters were:

- Dielectric material composition alone
- Dipole length and dipole placement in the "length" direction

A linear regression analysis further showed that dipole length and dielectric material composition were the two design parameters that had the most significant impact on the ratio of side lobe peak to main lobe peak for our FSS model.

## 5.2 Recommendations

The best measurement of a model's accuracy is a comparison with experimental measurements. Simple FSS structures with relatively few elements, such as an aluminum plate with nine slots, can be fabricated with varying tolerances and measured at a nominal cost. The variation of performance in the measured data could then be compared to the variation of performance as predicted by the model, to test the model's validity.

Adding to the complexity of the model would also be useful in discovering performance trends. Adding design parameters such as curved surfaces, different element shapes, and dielectric surface roughness would increase the versatility of the model, and an analysis of the impact of increasing the number of elements and dielectric layers would also aid in improving FSS design.

Finally, a top-level comparison of a tolerance-based model with different CEM codes (AIM, FISC, EMAP 5.0) would be beneficial in understanding how each code processes the same FSS with manufacturing errors, especially if the code outputs were compared to measured data from simple models.
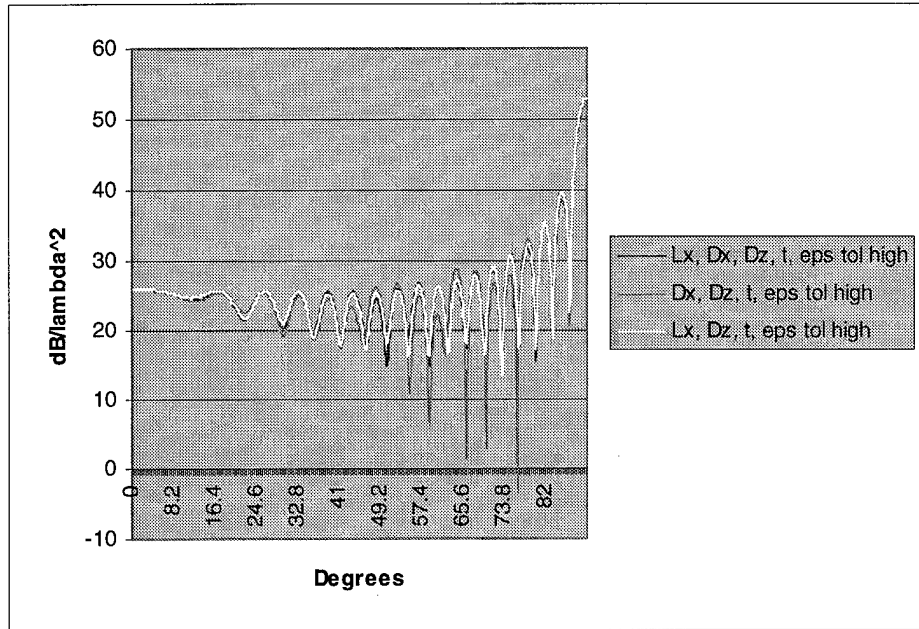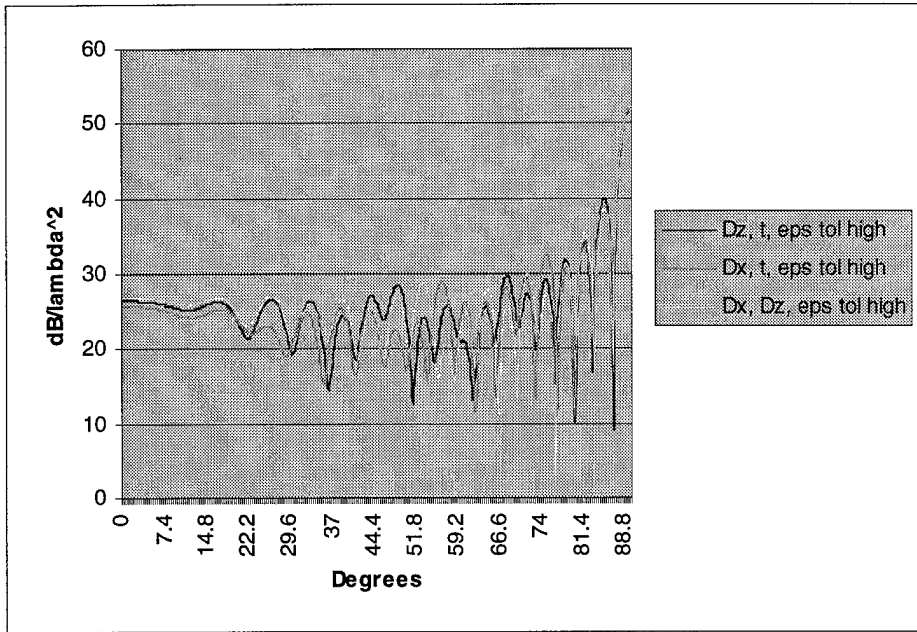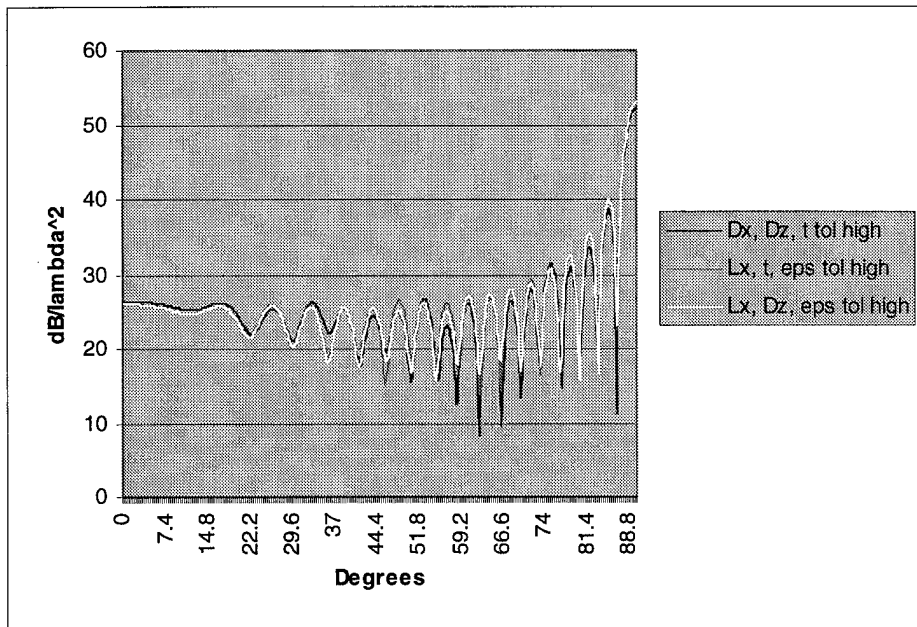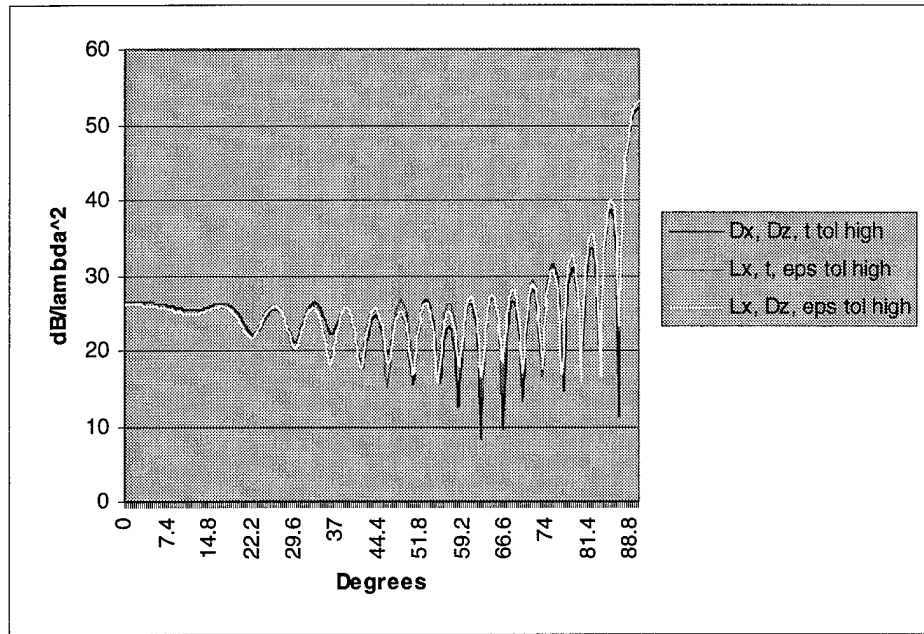
# APPENDIX A: DATA PLOTS AND TABLES

## A.1 Pattern Plots



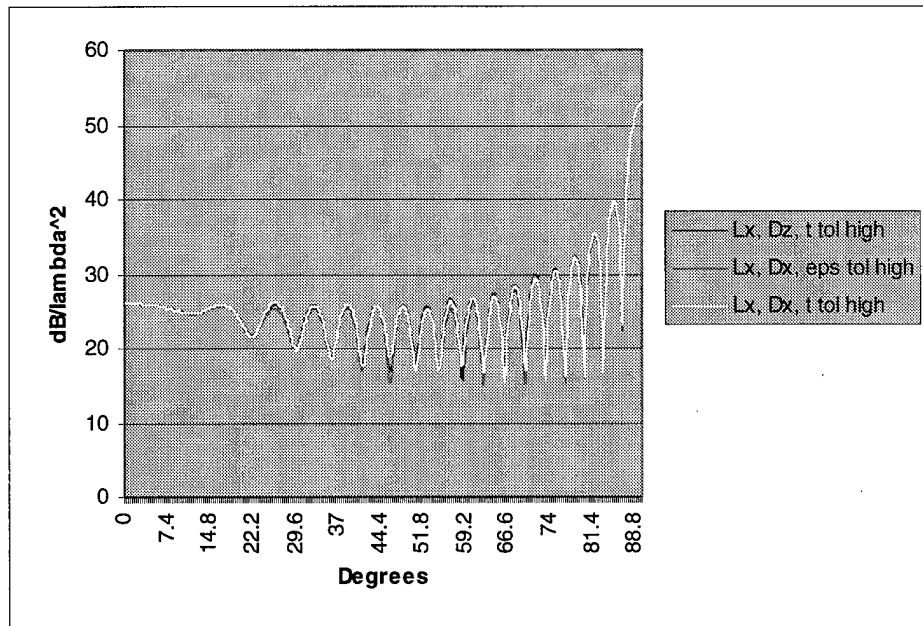**Figure A.1: Configurations 1, 2, and 3**

**Figure A.2: Configurations 4, 5, and 6**



**Figure A.3: Configurations 7, 8, and 9**
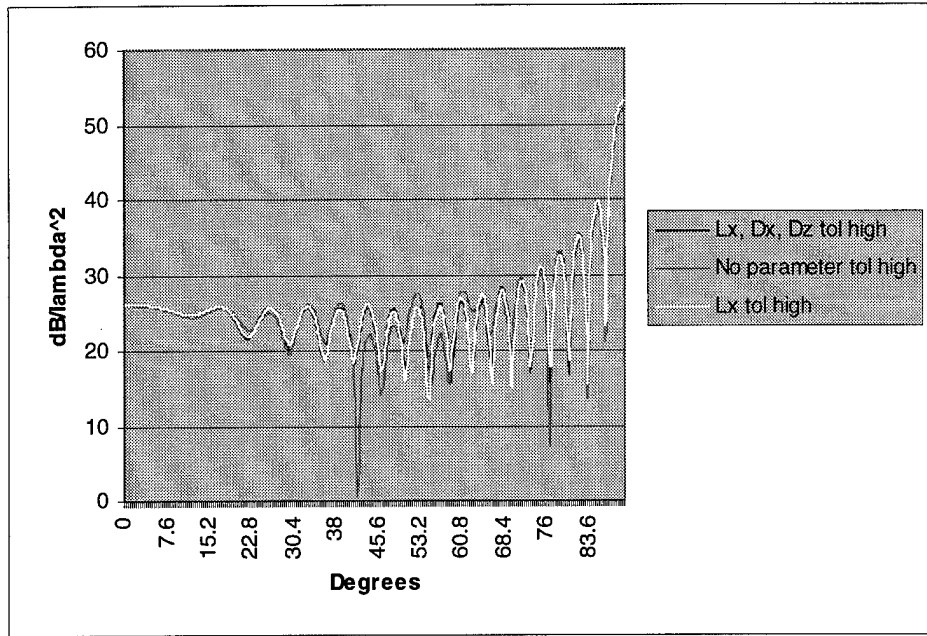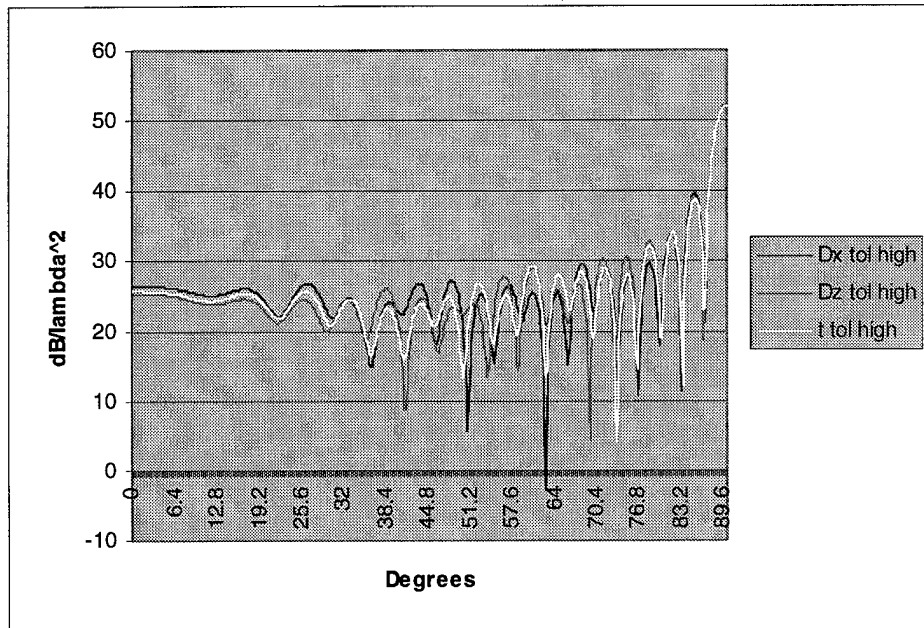
**Figure A.4: Configurations 10, 11, and 12**



**Figure A.5: Configurations 13, 14, and 15**

**Figure A.6: Configurations 16, 17, and 18**



**Figure A.7: Configurations 19, 20, and 21**
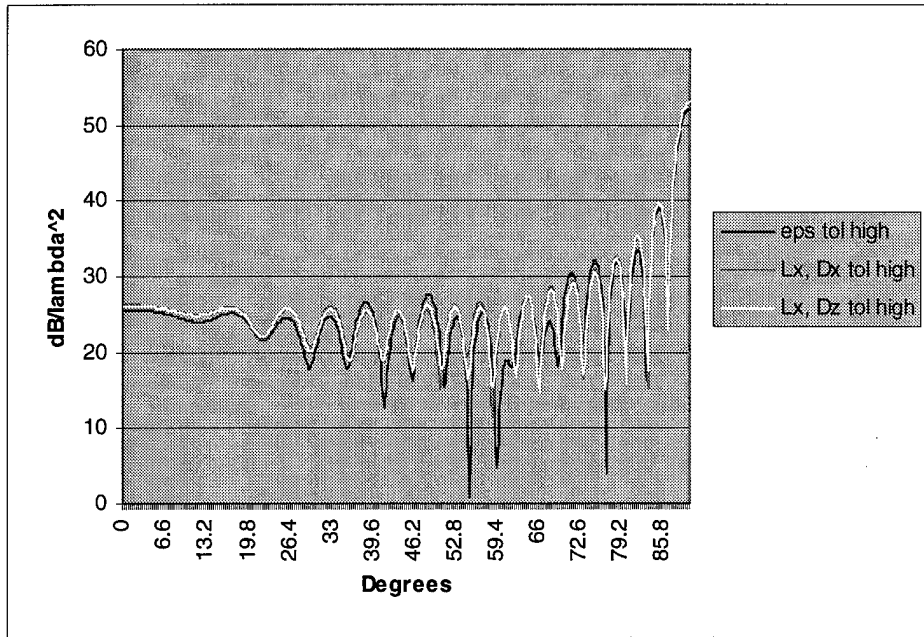
**Figure A.8: Configurations 22, 23, and 24**
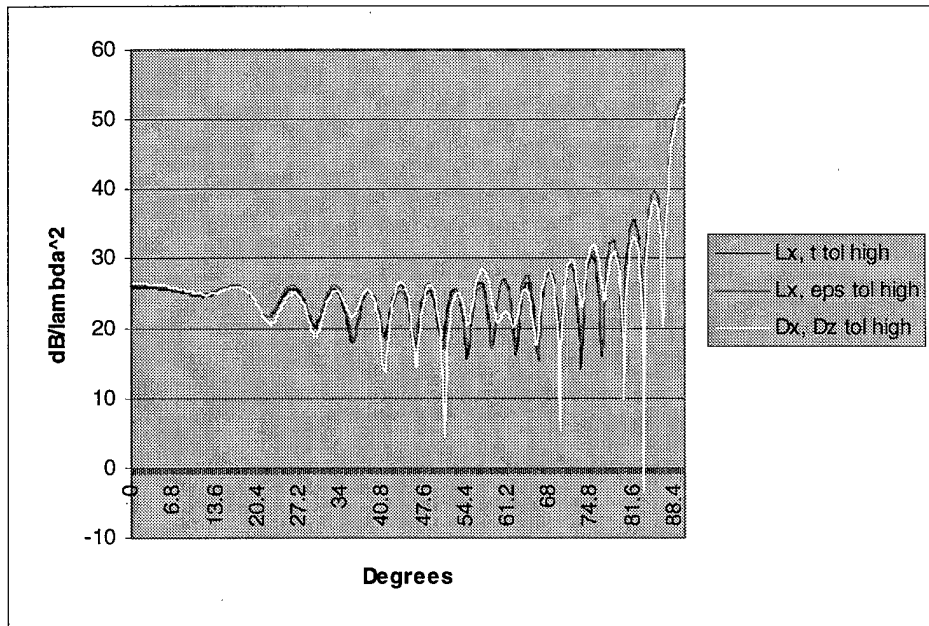


**Figure A.9: Configurations 25, 26, and 27**

47
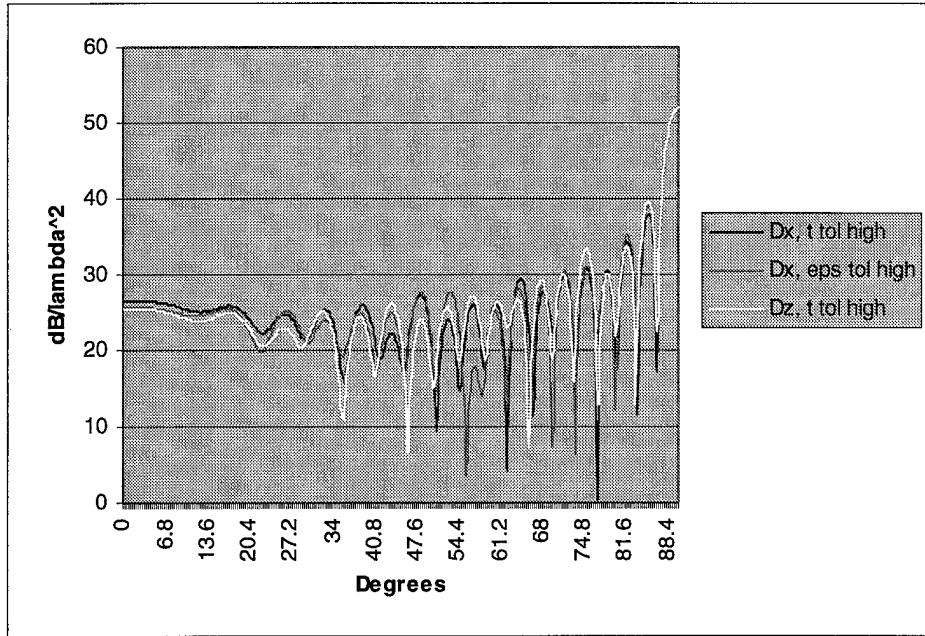
**Figure A.10: Configurations 28, 29, and 30**
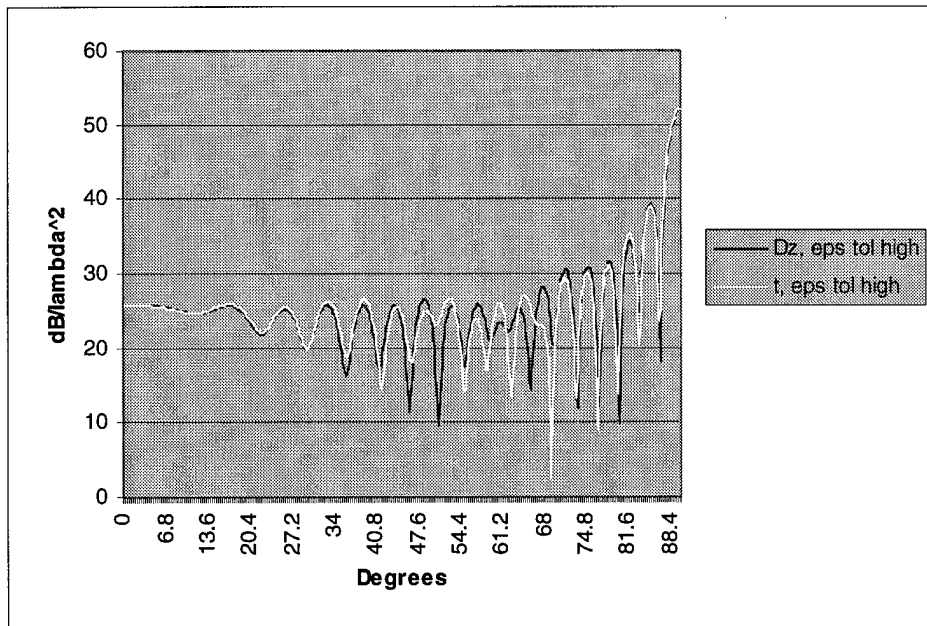


**Figure A.11: Configurations 31 and 32**

48

A.2 Scatter Plots

The following plots show the trends for each output performance parameter vs. each

input performance parameter, at both a high and low tolerance.
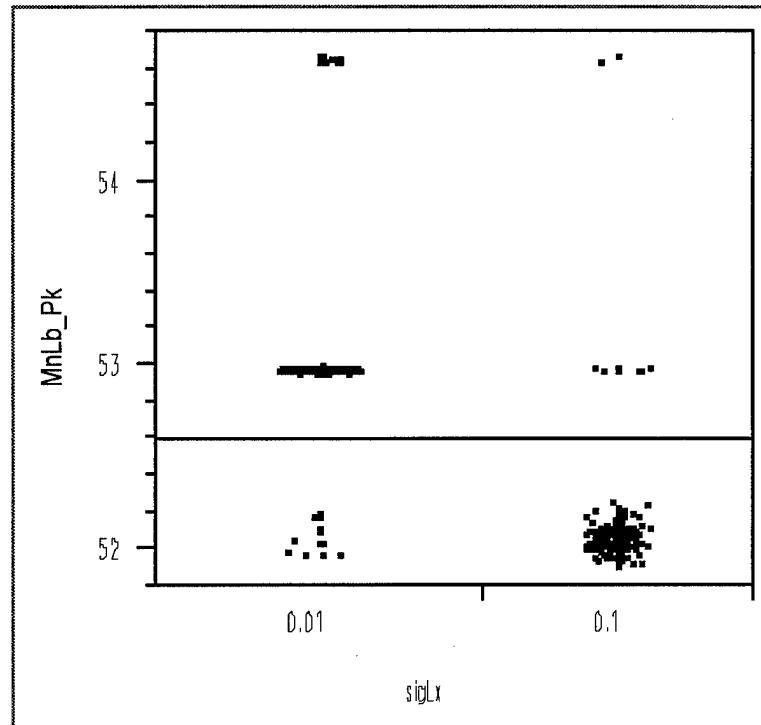


**Figure A.12: Main lobe peak by variation in dipole length**
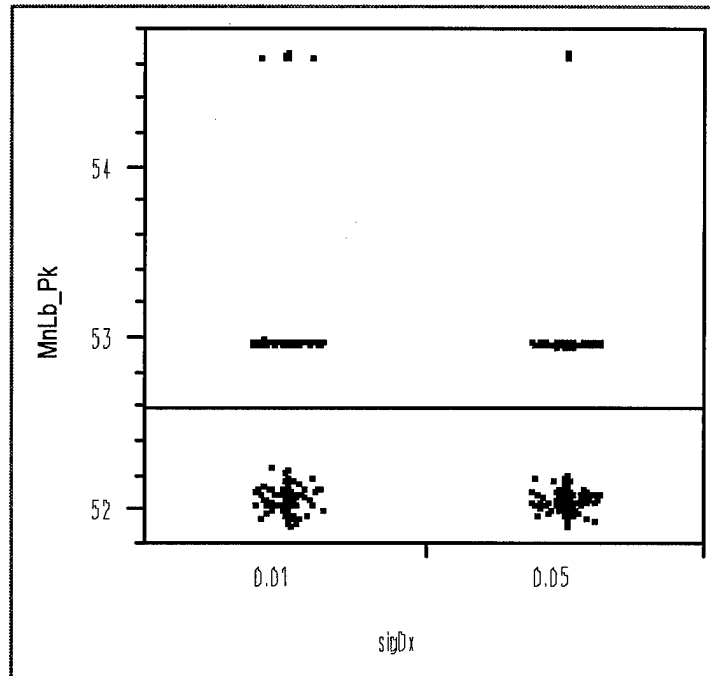
**Figure A.13:** Main lobe peak by variation of dipole placement in "length" direction
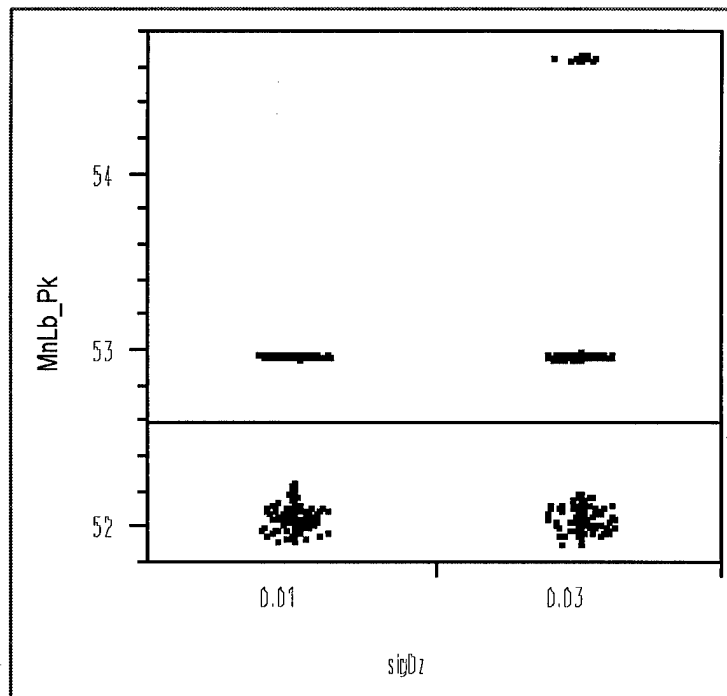


**Figure A.14:** Main lobe peak by variation of dipole placement in "width" direction

**Figure A.15:  Main lobe peak by variation of dielectric thickness**



**Figure A.16:  Main lobe peak by variation of dielectric constant**

51

**Figure A.17: Main lobe width by variation of dipole length**
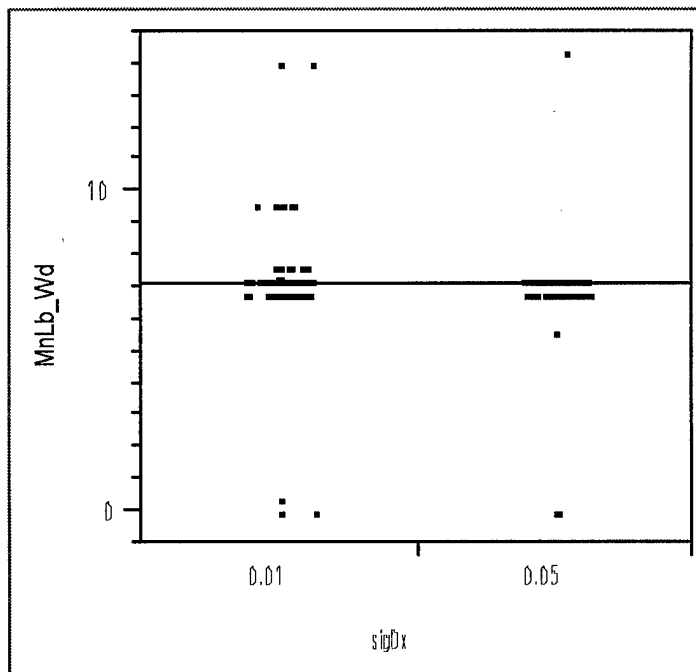


**Figure A.18: Main lobe width by variation of dipole placement in "length" direction**

52

**Figure A.19: Main lobe width by variation in dipole placement in "width" direction**



**Figure A.20: Main lobe width by variation in dielectric thickness**
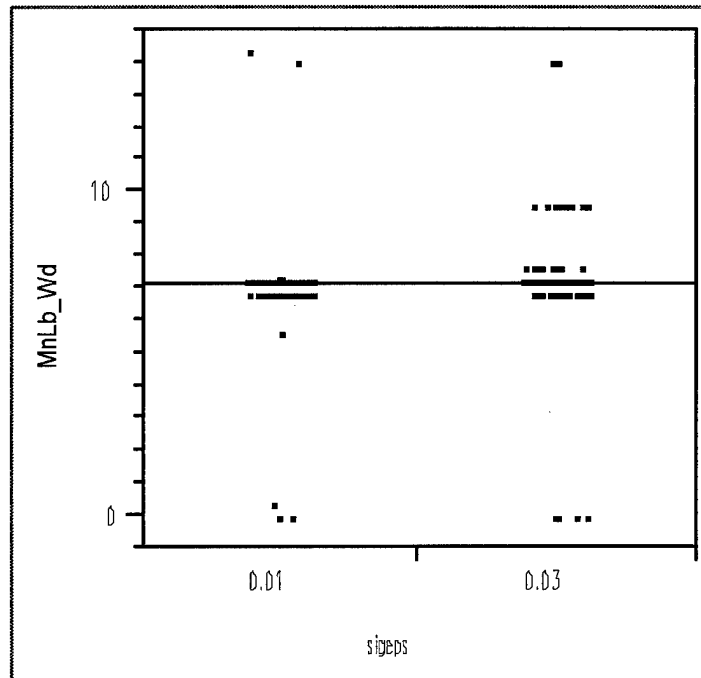
**Figure A.21: Main lobe width by variation of dielectric constant**



**Figure A.22: Side lobe peak by variation of dipole length**

54

**Figure A.23: Side lobe peak by variation of dipole placement in "length" direction**
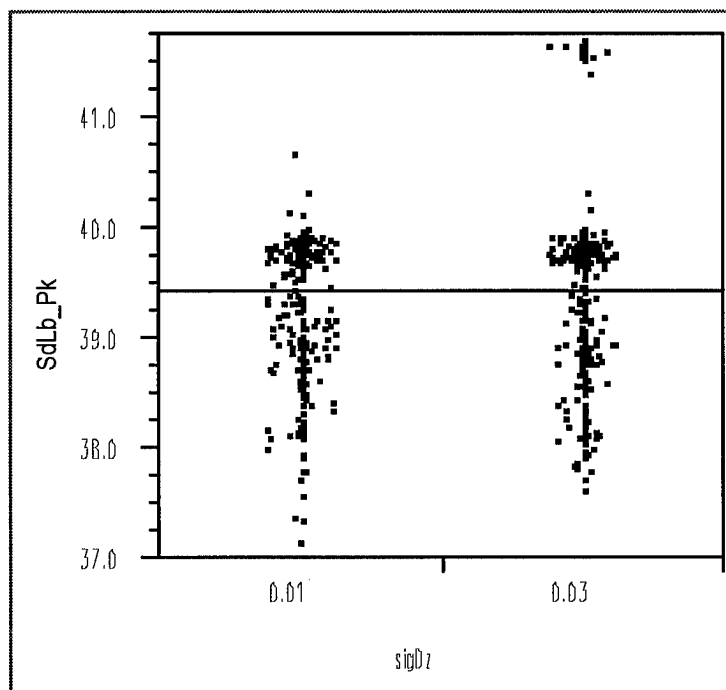


**Figure A.24: Side lobe peak by variation of dipole placement in "width" direction**

**Figure A.25: Side lobe peak by variation in dielectric thickness**



**Figure A.26: Side lobe peak by variation in dielectric constant**
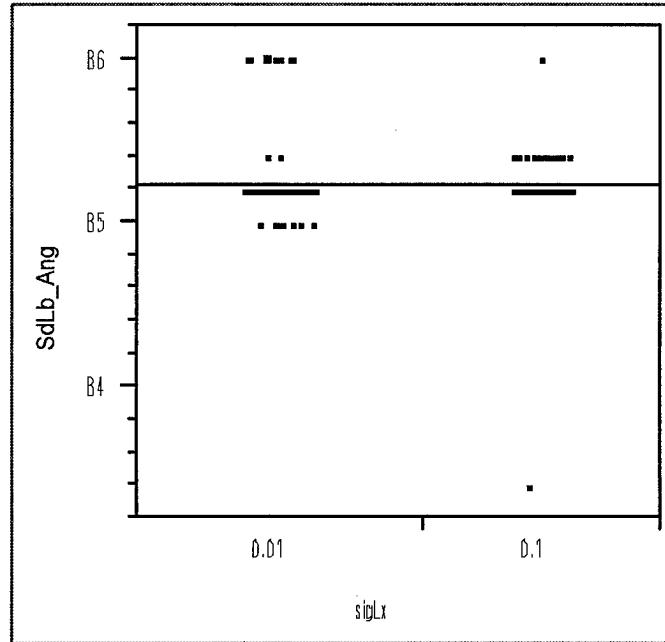
**Figure A.27: Side lobe angle by variation of dipole length**
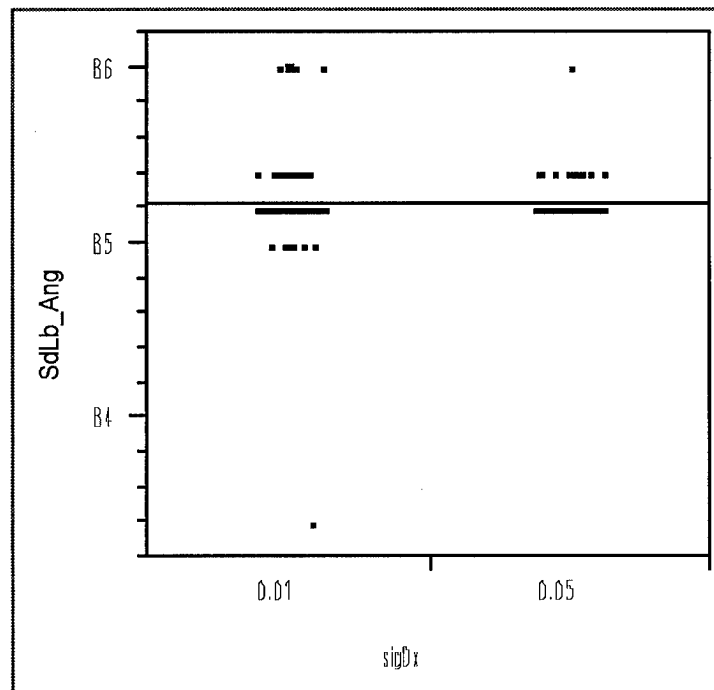


**Figure A.28: Side lobe angle by variation of dipole placement in "length" direction**
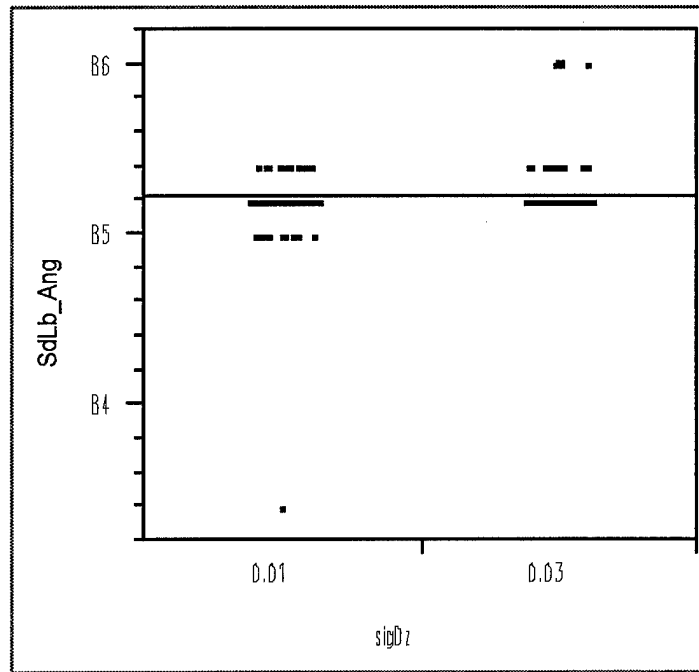
**Figure A.29: Side lobe angle by variation of dipole placement in "width" direction**
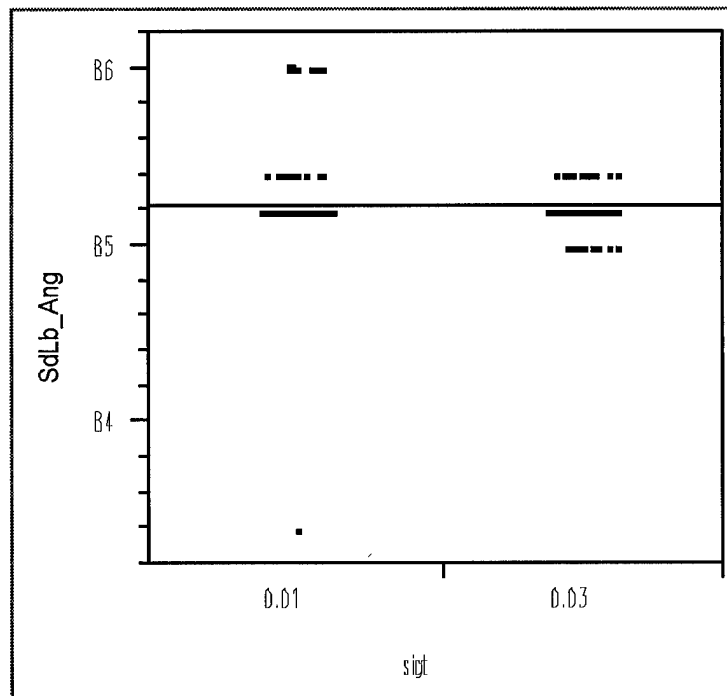


**Figure A.30: Side lobe angle by variation of dielectric thickness**

58
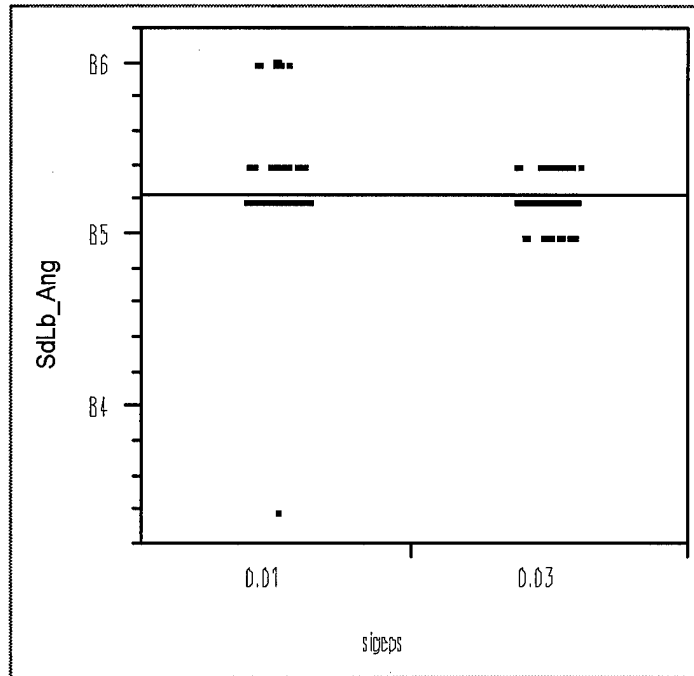
**Figure A.31: Side lobe angle by variation of dielectric constant**
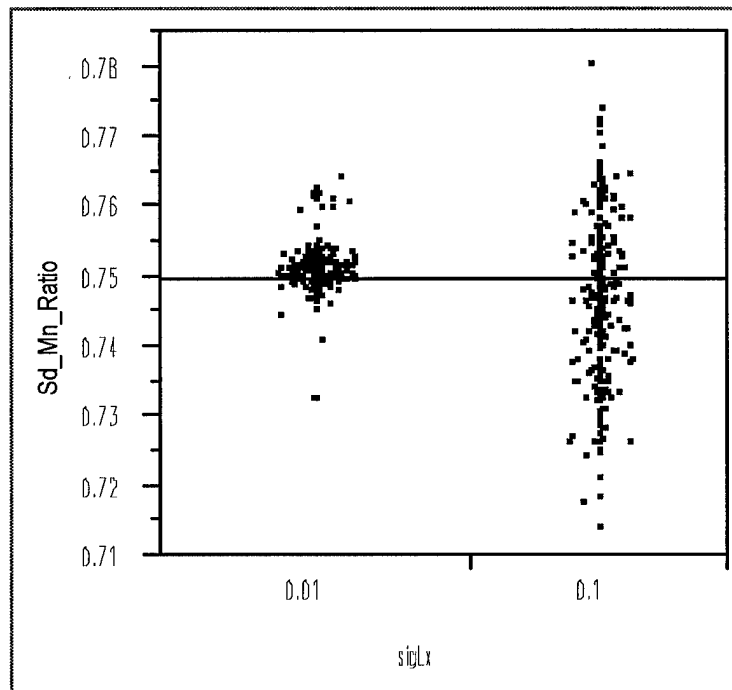


**Figure A.32: Side/Main lobe ratio by variation of dipole length**

59
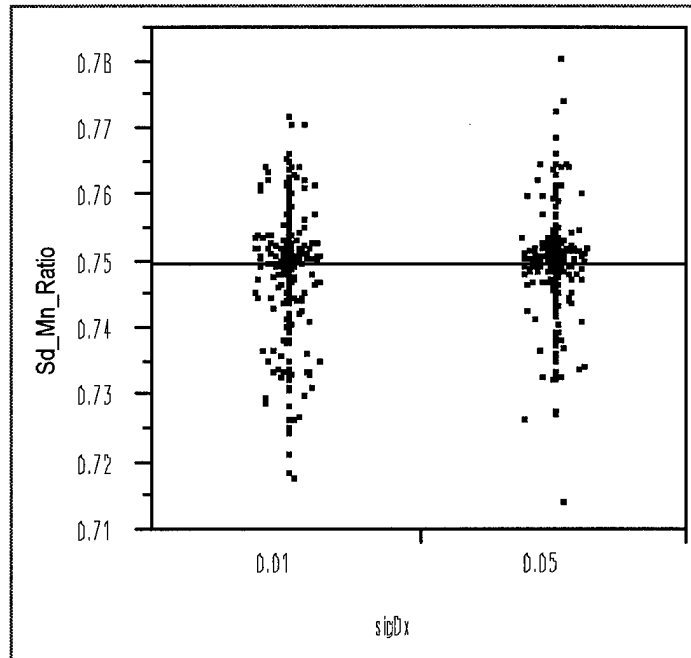
**Figure A.33: Side/Main lobe ratio by variation of dipole placement in "length" direction**
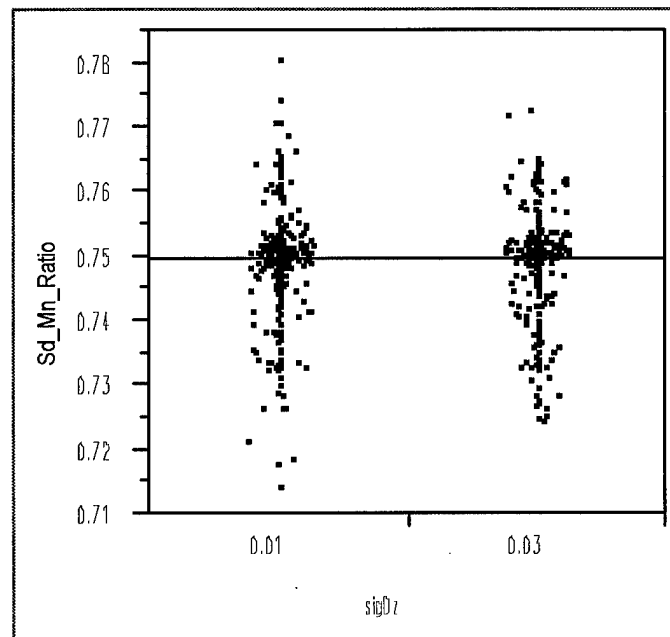


**Figure A.34: Side/Main lobe ratio by variation of dipole placement in "width" direction**
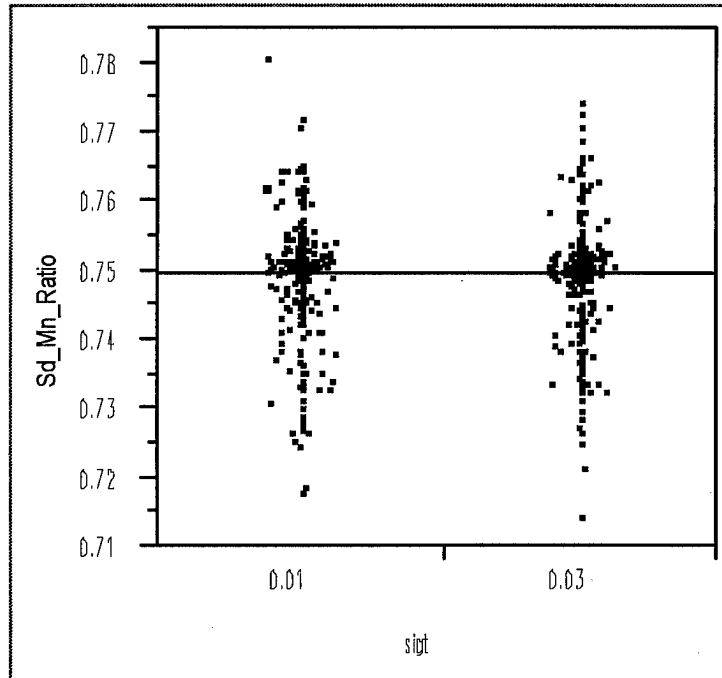
**Figure A.35: Side/Main lobe ratio by variation of dielectric thickness**
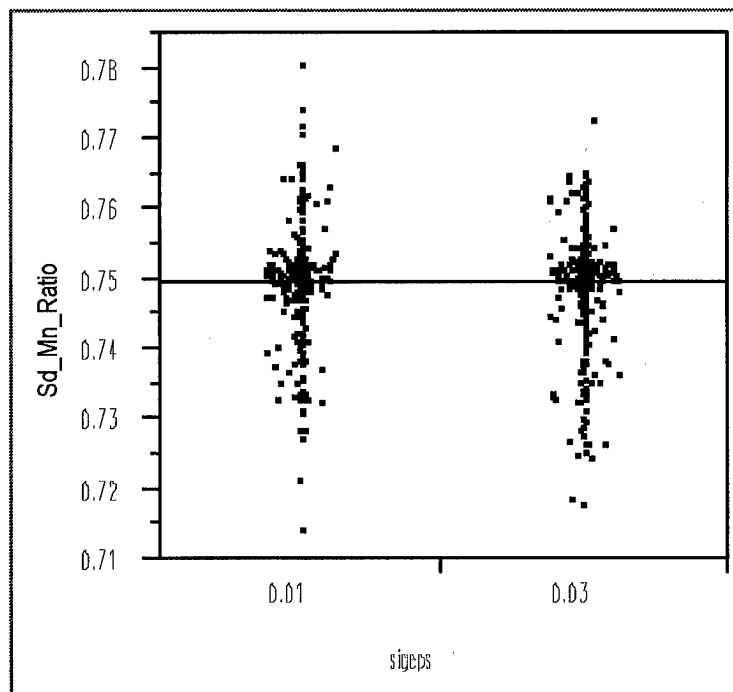


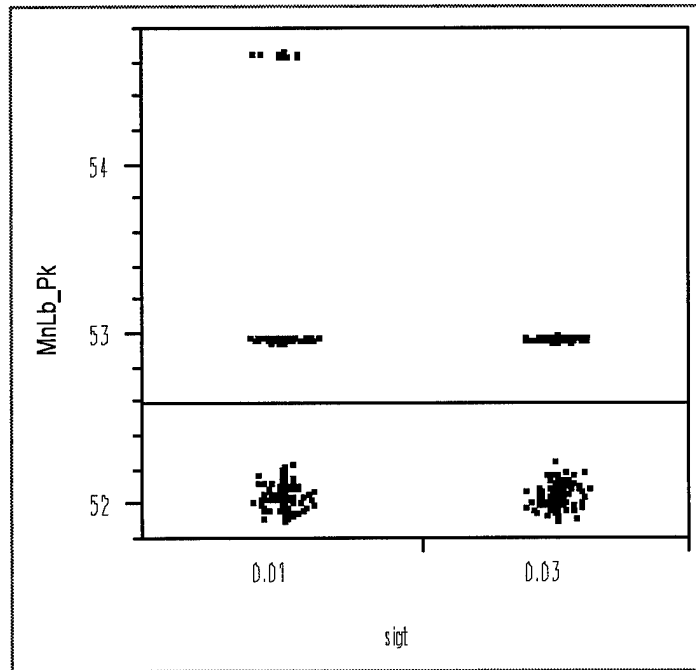**Figure A.36: Side/Main lobe ratio by variation of dielectric constant**
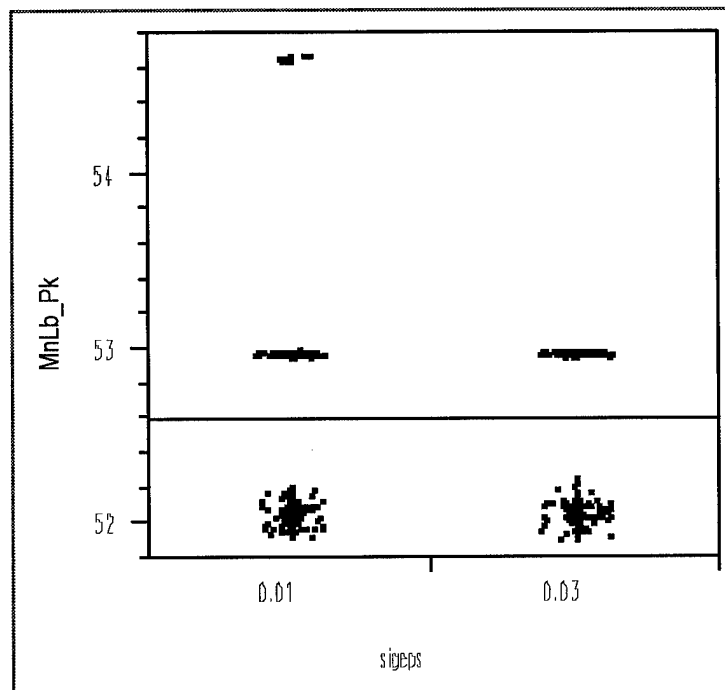
61
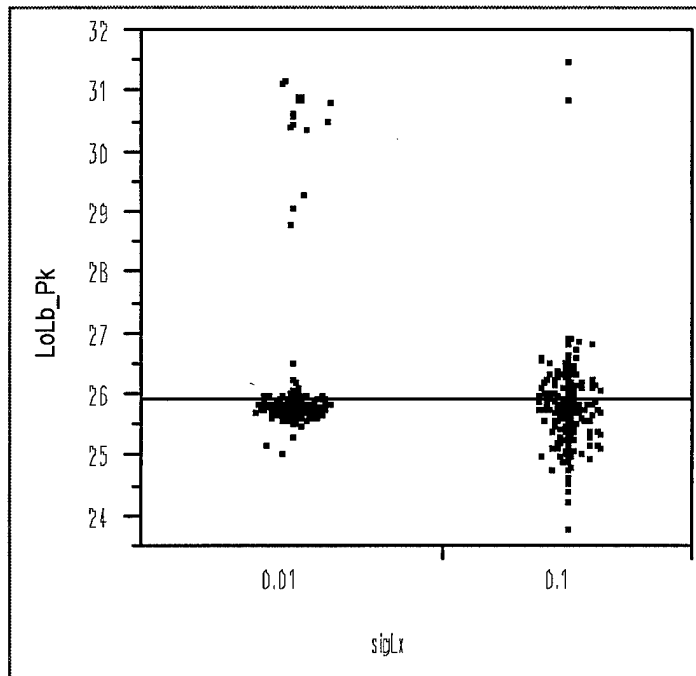
**Figure A.37: Low lobe peak by variation of dipole length**
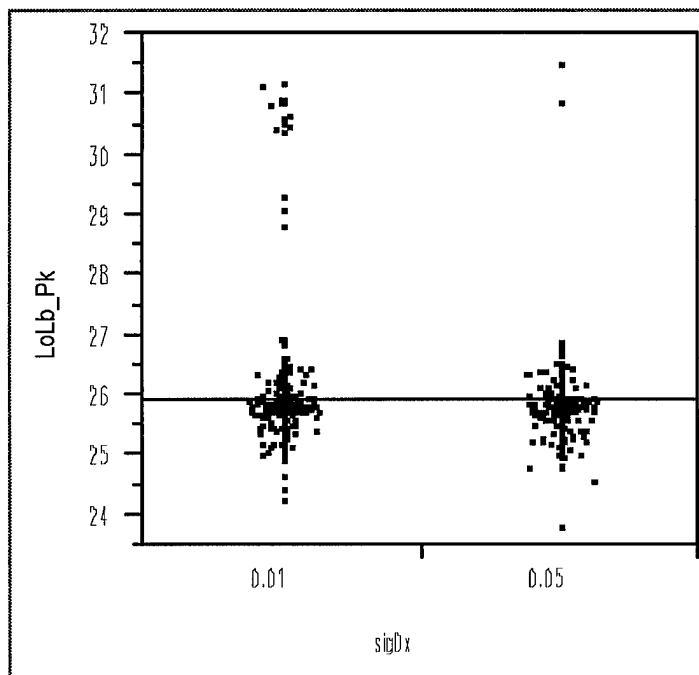


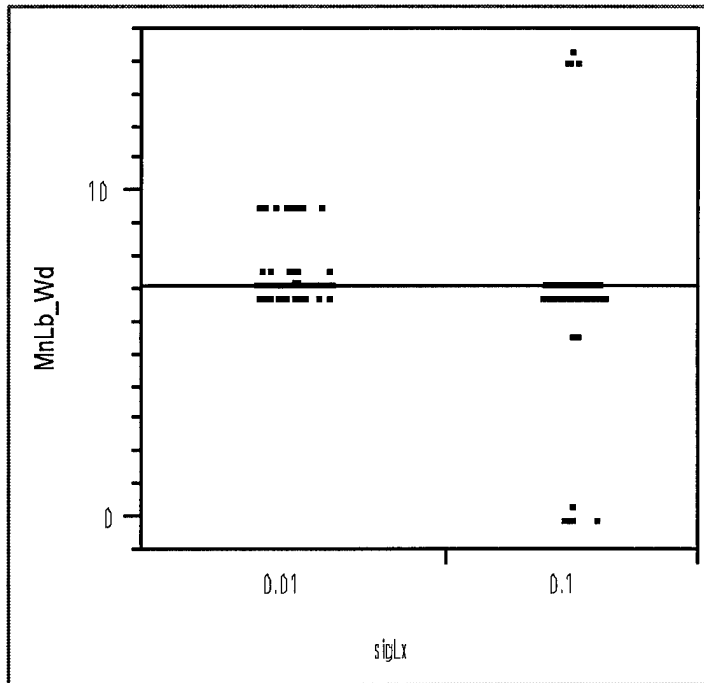**Figure A.38: Low lobe peak by variation of dipole placement in "length" direction**
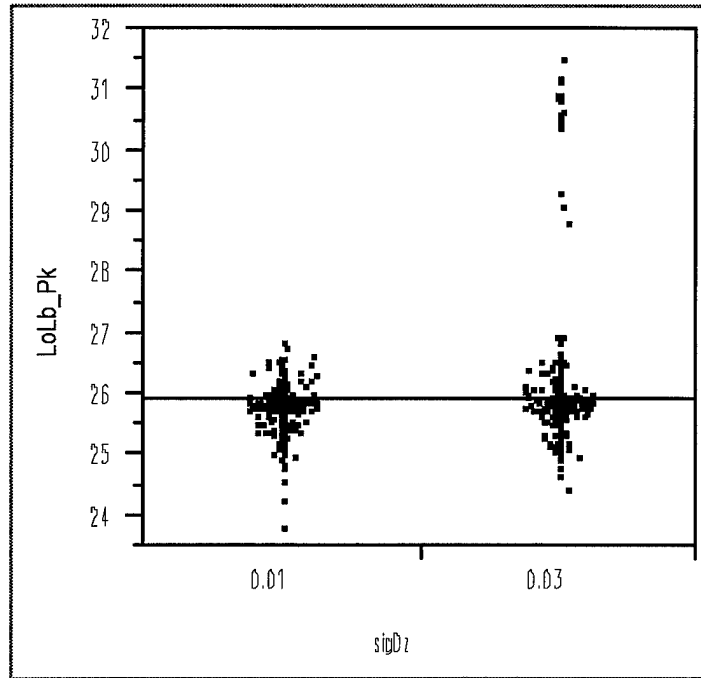
**Figure A.39: Low lobe peak by dipole placement in "width" direction**
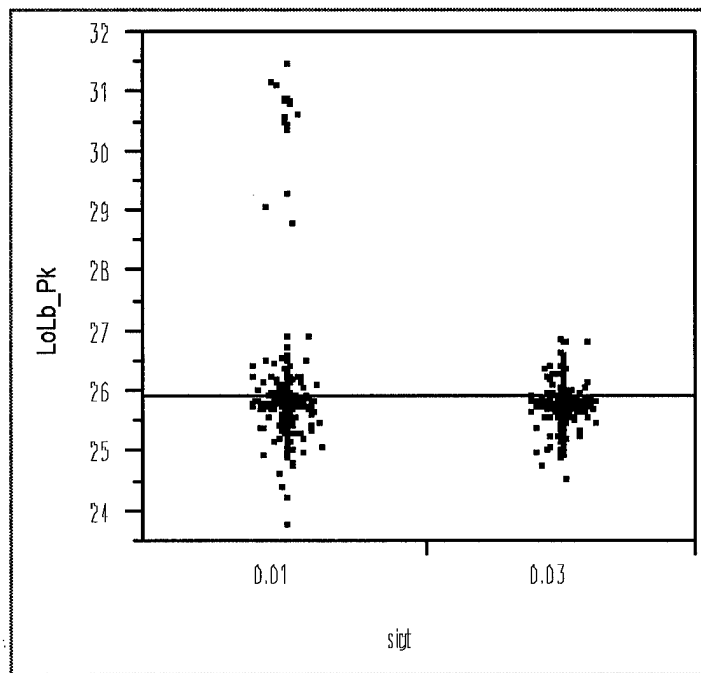


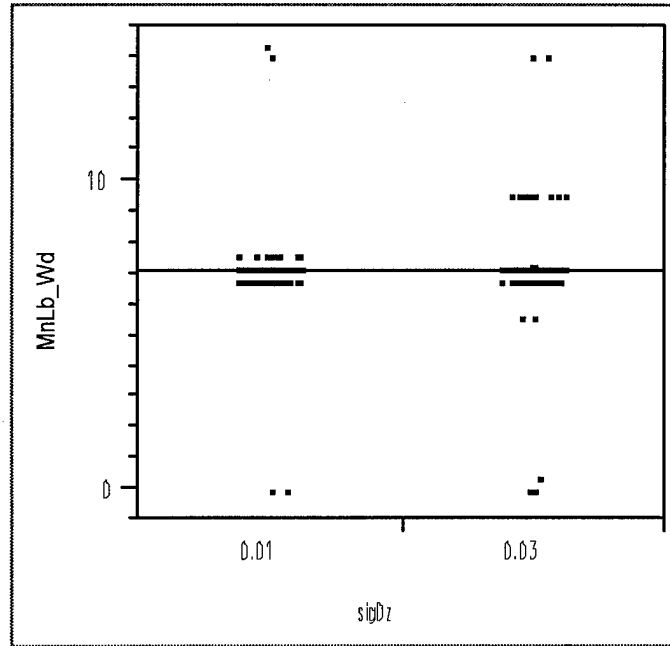**Figure A.40: Low lobe peak by variation of dielectric thickness**
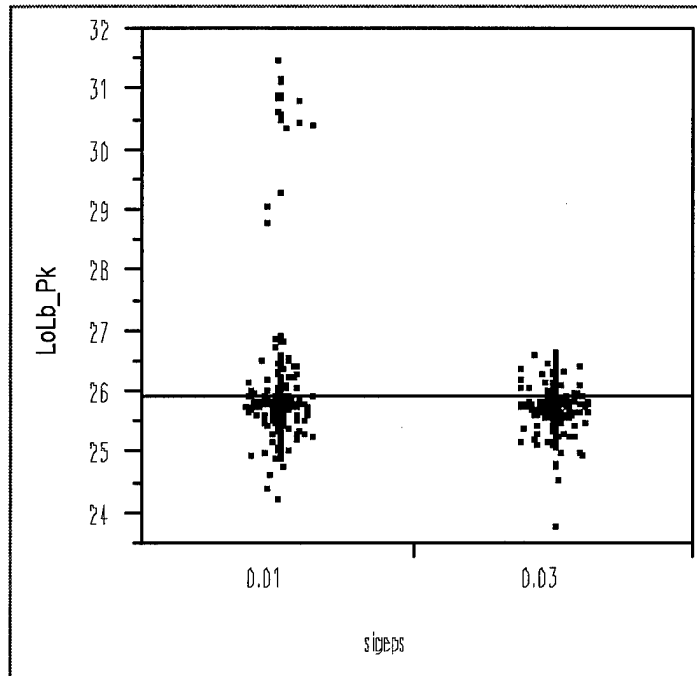
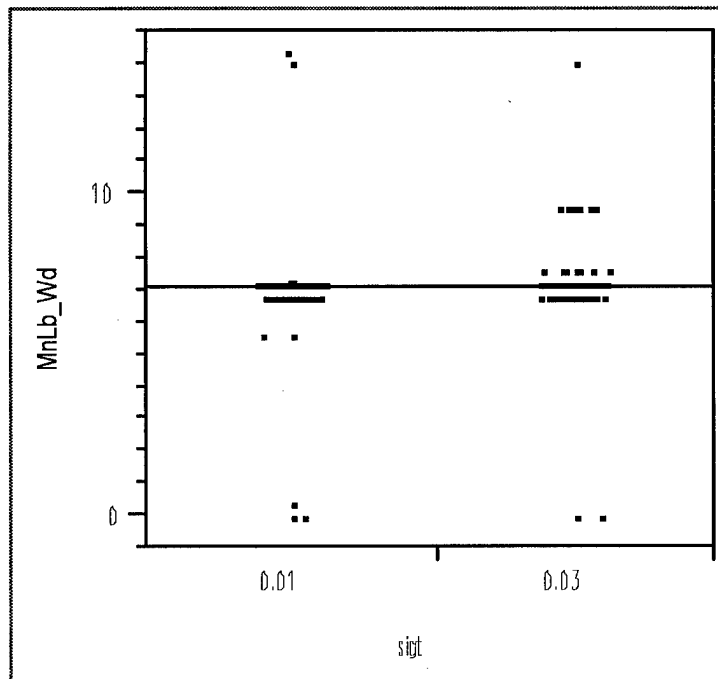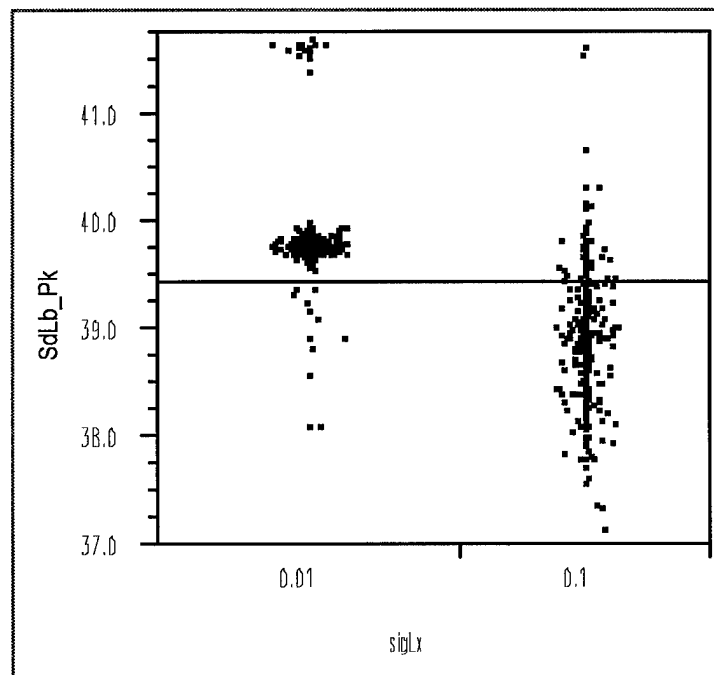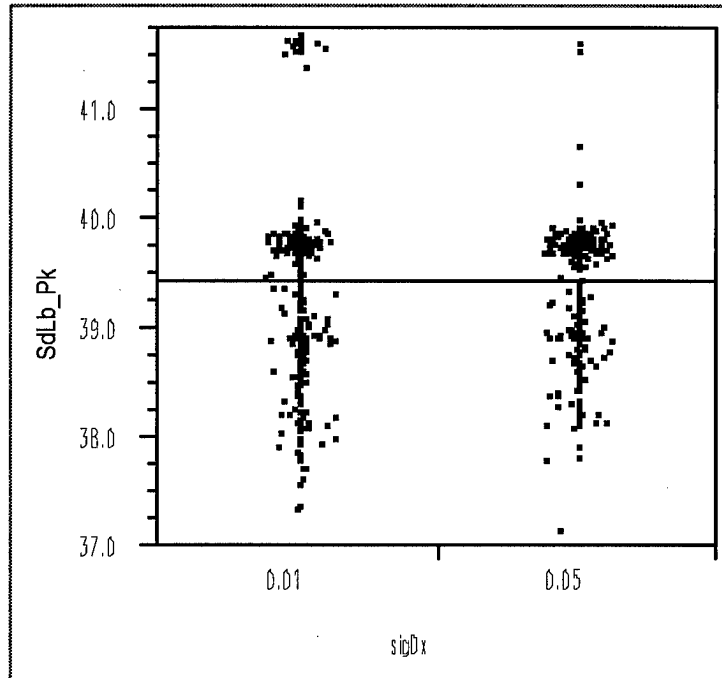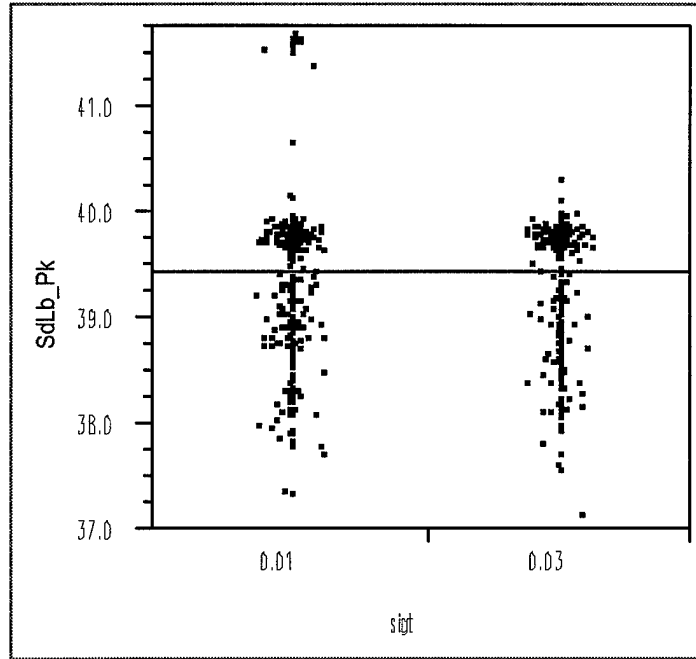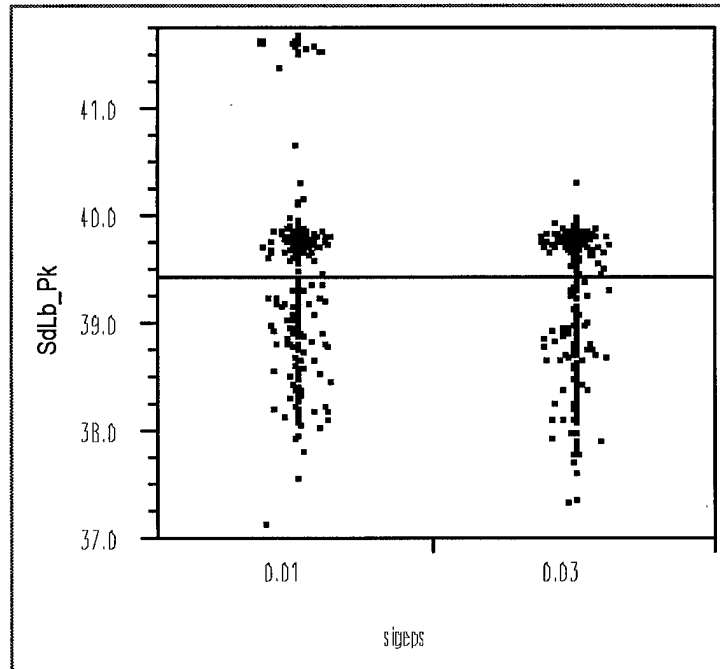**Figure A.41: Low lobe peak by variation of dielectric constant**

## A.3 Statistical Analysis Tables

The following are the statistical analysis tables for each of the performance parameters.

Response: MnLb_Pk

### Summary of Fit

| | |
|---|---|
| RSquare | 0.802144 |
| RSquare Adj | 0.793111 |
| Root Mean Square Error | 0.247779 |
| Mean of Response | 52.60545 |

### Effect Test

| Source | Nparm | DF | Sum of Squares | F Ratio | Prob>F |
|---|---|---|---|---|---|
| sigLx | 1 | 1 | 141.15052 | 2299.083 | <.0001 |
| sigDx | 1 | 1 | 0.00991 | 0.1614 | 0.6880 |
| sigLx*sigDx | 1 | 1 | 0.57018 | 9.2872 | 0.0024 |
| sigDz | 1 | 1 | 2.10417 | 34.2731 | <.0001 |
| sigLx*sigDz | 1 | 1 | 0.34878 | 5.6809 | 0.0174 |
| sigDx*sigDz | 1 | 1 | 0.33164 | 5.4018 | 0.0204 |
| sigLx*sigDx*sigDz | 1 | 1 | 2.22206 | 36.1933 | <.0001 |
| sigt | 1 | 1 | 0.61178 | 9.9648 | 0.0017 |
| sigLx*sigt | 1 | 1 | 0.04951 | 0.8064 | 0.3695 |
| sigDx*sigt | 1 | 1 | 0.02735 | 0.4456 | 0.5047 |
| sigLx*sigDx*sigt | 1 | 1 | 0.53578 | 8.7269 | 0.0032 |
| sigDz*sigt | 1 | 1 | 2.20416 | 35.9017 | <.0001 |
| sigLx*sigDz*sigt | 1 | 1 | 0.35965 | 5.8580 | 0.0158 |
| sigDx*sigDz*sigt | 1 | 1 | 0.37539 | 6.1144 | 0.0137 |
| sigLx*sigDx*sigDz*sigt | 1 | 1 | 2.08196 | 33.9114 | <.0001 |
| sigeps | 1 | 1 | 0.54322 | 8.8480 | 0.0030 |
| sigLx*sigeps | 1 | 1 | 0.02747 | 0.4474 | 0.5038 |
| sigDx*sigeps | 1 | 1 | 0.01653 | 0.2693 | 0.6040 |
| sigLx*sigDx*sigeps | 1 | 1 | 0.49231 | 8.0188 | 0.0048 |
| sigDz*sigeps | 1 | 1 | 2.14518 | 34.9411 | <.0001 |
| sigLx*sigDz*sigeps | 1 | 1 | 0.35701 | 5.8150 | 0.0162 |
| sigDx*sigDz*sigeps | 1 | 1 | 0.31826 | 5.1839 | 0.0231 |
| sigLx*sigDx*sigDz*sigeps | 1 | 1 | 2.25498 | 36.7296 | <.0001 |
| sigt*sigeps | 1 | 1 | 0.48582 | 7.9131 | 0.0050 |
| sigLx*sigt*sigeps | 1 | 1 | 0.01592 | 0.2594 | 0.6107 |
| sigDx*sigt*sigeps | 1 | 1 | 0.04963 | 0.8084 | 0.3689 |
| sigLx*sigDx*sigt*sigeps | 1 | 1 | 0.60355 | 9.8307 | 0.0018 |
| sigDz*sigt*sigeps | 1 | 1 | 2.17370 | 35.4057 | <.0001 |
| sigLx*sigDz*sigt*sigeps | 1 | 1 | 0.35444 | 5.7731 | 0.0165 |
| sigDx*sigDz*sigt*sigeps | 1 | 1 | 0.30072 | 4.8982 | 0.0272 |
| sigLx*sigDx*sigDz*sigt*sigeps | 1 | 1 | 2.29179 | 37.3291 | <.0001 |

**Figure A.42:  Parameter Impact Analysis Table--Main Lobe Peak**

Response: MnLb_Wd

Summary of Fit

| | |
|---|---|
| RSquare | 0.24637 |
| RSquare Adj | 0.211962 |
| Root Mean Square Error | 0.897661 |
| Mean of Response | 7.161744 |

Effect Test

| Source | Nparm | DF | Sum of Squares | F Ratio | Prob>F |
|---|---|---|---|---|---|
| sigLx | 1 | 1 | 25.904879 | 32.1482 | <.0001 |
| sigDx | 1 | 1 | 3.901657 | 4.8420 | 0.0281 |
| sigLx*sigDx | 1 | 1 | 5.344192 | 6.6322 | 0.0102 |
| sigDz | 1 | 1 | 2.761079 | 3.4265 | 0.0646 |
| sigLx*sigDz | 1 | 1 | 4.434517 | 5.5033 | 0.0193 |
| sigDx*sigDz | 1 | 1 | 12.443468 | 15.4425 | <.0001 |
| sigLx*sigDx*sigDz | 1 | 1 | 0.087002 | 0.1080 | 0.7426 |
| sigt | 1 | 1 | 5.798022 | 7.1954 | 0.0075 |
| sigLx*sigt | 1 | 1 | 3.704719 | 4.5976 | 0.0324 |
| sigDx*sigt | 1 | 1 | 7.865508 | 9.7612 | 0.0019 |
| sigLx*sigDx*sigt | 1 | 1 | 2.850672 | 3.5377 | 0.0604 |
| sigDz*sigt | 1 | 1 | 7.376945 | 9.1549 | 0.0026 |
| sigLx*sigDz*sigt | 1 | 1 | 0.895609 | 1.1115 | 0.2921 |
| sigDx*sigDz*sigt | 1 | 1 | 3.221194 | 3.9975 | 0.0460 |
| sigLx*sigDx*sigDz*sigt | 1 | 1 | 2.596201 | 3.2219 | 0.0731 |
| sigeps | 1 | 1 | 4.328674 | 5.3719 | 0.0208 |
| sigLx*sigeps | 1 | 1 | 6.395854 | 7.9373 | 0.0050 |
| sigDx*sigeps | 1 | 1 | 15.287154 | 18.9715 | <.0001 |
| sigLx*sigDx*sigeps | 1 | 1 | 0.569547 | 0.7068 | 0.4008 |
| sigDz*sigeps | 1 | 1 | 2.386836 | 2.9621 | 0.0857 |
| sigLx*sigDz*sigeps | 1 | 1 | 3.387824 | 4.2043 | 0.0407 |
| sigDx*sigDz*sigeps | 1 | 1 | 5.879409 | 7.2964 | 0.0071 |
| sigLx*sigDx*sigDz*sigeps | 1 | 1 | 1.040793 | 1.2916 | 0.2561 |
| sigt*sigeps | 1 | 1 | 7.780903 | 9.6562 | 0.0020 |
| sigLx*sigt*sigeps | 1 | 1 | 2.263656 | 2.8092 | 0.0942 |
| sigDx*sigt*sigeps | 1 | 1 | 5.559637 | 6.8996 | 0.0088 |
| sigLx*sigDx*sigt*sigeps | 1 | 1 | 2.821413 | 3.5014 | 0.0617 |
| sigDz*sigt*sigeps | 1 | 1 | 0.713738 | 0.8858 | 0.3470 |
| sigLx*sigDz*sigt*sigeps | 1 | 1 | 9.405309 | 11.6721 | 0.0007 |
| sigDx*sigDz*sigt*sigeps | 1 | 1 | 2.233192 | 2.7714 | 0.0964 |
| sigLx*sigDx*sigDz*sigt*sigeps | 1 | 1 | 4.650438 | 5.7712 | 0.0166 |

**Figure A.43:  Parameter Impact Analysis Table--Main Lobe Width**

Response: SdLb_Pk

## Summary of Fit

| | |
|---|---|
| RSquare | 0.550891 |
| RSquare Adj | 0.530387 |
| Root Mean Square Error | 0.45963 |
| Mean of Response | 39.43243 |

## Effect Test

| Source | Nparm | DF | Sum of Squares | F Ratio | Prob>F |
|---|---|---|---|---|---|
| sigLx | 1 | 1 | 139.08923 | 658.3802 | <.0001 |
| sigDx | 1 | 1 | 0.55095 | 2.6079 | 0.1068 |
| sigLx*sigDx | 1 | 1 | 2.95587 | 13.9916 | 0.0002 |
| sigDz | 1 | 1 | 1.06028 | 5.0188 | 0.0254 |
| sigLx*sigDz | 1 | 1 | 1.03688 | 4.9081 | 0.0271 |
| sigDx*sigDz | 1 | 1 | 0.24104 | 1.1410 | 0.2858 |
| sigLx*sigDx*sigDz | 1 | 1 | 2.25705 | 10.6838 | 0.0011 |
| sigt | 1 | 1 | 0.42609 | 2.0169 | 0.1560 |
| sigLx*sigt | 1 | 1 | 0.04407 | 0.2086 | 0.6480 |
| sigDx*sigt | 1 | 1 | 0.19536 | 0.9248 | 0.3366 |
| sigLx*sigDx*sigt | 1 | 1 | 1.68033 | 7.9539 | 0.0049 |
| sigDz*sigt | 1 | 1 | 0.99236 | 4.6974 | 0.0306 |
| sigLx*sigDz*sigt | 1 | 1 | 0.80322 | 3.8020 | 0.0516 |
| sigDx*sigDz*sigt | 1 | 1 | 0.05854 | 0.2771 | 0.5988 |
| sigLx*sigDx*sigDz*sigt | 1 | 1 | 3.12939 | 14.8130 | 0.0001 |
| sigeps | 1 | 1 | 1.89647 | 8.9769 | 0.0028 |
| sigLx*sigeps | 1 | 1 | 0.49507 | 2.3434 | 0.1263 |
| sigDx*sigeps | 1 | 1 | 0.17742 | 0.8398 | 0.3598 |
| sigLx*sigDx*sigeps | 1 | 1 | 0.11973 | 0.5667 | 0.4518 |
| sigDz*sigeps | 1 | 1 | 0.68004 | 3.2190 | 0.0732 |
| sigLx*sigDz*sigeps | 1 | 1 | 1.27652 | 6.0424 | 0.0142 |
| sigDx*sigDz*sigeps | 1 | 1 | 0.00119 | 0.0056 | 0.9402 |
| sigLx*sigDx*sigDz*sigeps | 1 | 1 | 4.27620 | 20.2414 | <.0001 |
| sigt*sigeps | 1 | 1 | 1.97228 | 9.3358 | 0.0023 |
| sigLx*sigt*sigeps | 1 | 1 | 0.30335 | 1.4359 | 0.2312 |
| sigDx*sigt*sigeps | 1 | 1 | 0.05776 | 0.2734 | 0.6012 |
| sigLx*sigDx*sigt*sigeps | 1 | 1 | 0.37418 | 1.7712 | 0.1837 |
| sigDz*sigt*sigeps | 1 | 1 | 2.54666 | 12.0546 | 0.0005 |
| sigLx*sigDz*sigt*sigeps | 1 | 1 | 0.40013 | 1.8940 | 0.1692 |
| sigDx*sigDz*sigt*sigeps | 1 | 1 | 0.51146 | 2.4210 | 0.1202 |
| sigLx*sigDx*sigDz*sigt*sigeps | 1 | 1 | 1.96783 | 9.3147 | 0.0024 |

**Figure A.44: Parameter Impact Analysis Table--Side Lobe Peak**

Response: SdLb_Ang

Summary of Fit

| | |
|---|---|
| RSquare | 0.334645 |
| RSquare Adj | 0.304268 |
| Root Mean Square Error | 0.124598 |
| Mean of Response | 85.22897 |

Effect Test

| Source | Nparm | DF | Sum of Squares | F Ratio | Prob>F |
|---|---|---|---|---|---|
| sigLx | 1 | 1 | 0.10994609 | 7.0820 | 0.0080 |
| sigDx | 1 | 1 | 0.03370380 | 2.1710 | 0.1411 |
| sigLx*sigDx | 1 | 1 | 0.07868567 | 5.0684 | 0.0247 |
| sigDz | 1 | 1 | 0.20603059 | 13.2711 | 0.0003 |
| sigLx*sigDz | 1 | 1 | 0.20282668 | 13.0647 | 0.0003 |
| sigDx*sigDz | 1 | 1 | 0.24441460 | 15.7435 | <.0001 |
| sigLx*sigDx*sigDz | 1 | 1 | 0.16800629 | 10.8218 | 0.0011 |
| sigt | 1 | 1 | 0.30580492 | 19.6979 | <.0001 |
| sigLx*sigt | 1 | 1 | 0.16898560 | 10.8849 | 0.0010 |
| sigDx*sigt | 1 | 1 | 0.10245950 | 6.5997 | 0.0104 |
| sigLx*sigDx*sigt | 1 | 1 | 0.41471274 | 26.7130 | <.0001 |
| sigDz*sigt | 1 | 1 | 0.09558953 | 6.1572 | 0.0133 |
| sigLx*sigDz*sigt | 1 | 1 | 0.00904665 | 0.5827 | 0.4455 |
| sigDx*sigDz*sigt | 1 | 1 | 0.04795789 | 3.0891 | 0.0793 |
| sigLx*sigDx*sigDz*sigt | 1 | 1 | 0.03433482 | 2.2116 | 0.1374 |
| sigeps | 1 | 1 | 0.17549382 | 11.3041 | 0.0008 |
| sigLx*sigeps | 1 | 1 | 0.29719405 | 19.1432 | <.0001 |
| sigDx*sigeps | 1 | 1 | 0.06914292 | 4.4537 | 0.0352 |
| sigLx*sigDx*sigeps | 1 | 1 | 0.49157554 | 31.6639 | <.0001 |
| sigDz*sigeps | 1 | 1 | 0.06227352 | 4.0112 | 0.0456 |
| sigLx*sigDz*sigeps | 1 | 1 | 0.02394535 | 1.5424 | 0.2147 |
| sigDx*sigDz*sigeps | 1 | 1 | 0.07424569 | 4.7824 | 0.0291 |
| sigLx*sigDx*sigDz*sigeps | 1 | 1 | 0.01737357 | 1.1191 | 0.2905 |
| sigt*sigeps | 1 | 1 | 0.05876978 | 3.7855 | 0.0521 |
| sigLx*sigt*sigeps | 1 | 1 | 0.04913795 | 3.1651 | 0.0757 |
| sigDx*sigt*sigeps | 1 | 1 | 0.00073249 | 0.0472 | 0.8281 |
| sigLx*sigDx*sigt*sigeps | 1 | 1 | 0.19099614 | 12.3027 | 0.0005 |
| sigDz*sigt*sigeps | 1 | 1 | 0.37061630 | 23.8726 | <.0001 |
| sigLx*sigDz*sigt*sigeps | 1 | 1 | 0.08731205 | 5.6240 | 0.0180 |
| sigDx*sigDz*sigt*sigeps | 1 | 1 | 0.34665306 | 22.3290 | <.0001 |
| sigLx*sigDx*sigDz*sigt*sigeps | 1 | 1 | 0.09953789 | 6.4115 | 0.0116 |

**Figure A.45: Parameter Impact Analysis Table: Side Lobe Angle**

Response: Sd_Mn_Ratio

Summary of Fit

RSquare                          0.141314
RSquare Adj                       0.10211
Root Mean Square Error           0.007422
Mean of Response                 0.749561

Effect Test

| Source | Nparm | DF | Sum of Squares | F Ratio | Prob>F |
|---|---|---|---|---|---|
| sigLx | 1 | 1 | 0.00301825 | 54.7898 | <.0001 |
| sigDx | 1 | 1 | 0.00016977 | 3.0818 | 0.0796 |
| sigLx*sigDx | 1 | 1 | 0.00047797 | 8.6766 | 0.0033 |
| sigDz | 1 | 1 | 0.00000194 | 0.0353 | 0.8511 |
| sigLx*sigDz | 1 | 1 | 0.00011749 | 2.1328 | 0.1446 |
| sigDx*sigDz | 1 | 1 | 0.00000088 | 0.0161 | 0.8992 |
| sigLx*sigDx*sigDz | 1 | 1 | 0.00005060 | 0.9186 | 0.3382 |
| sigt | 1 | 1 | 0.00000102 | 0.0184 | 0.8920 |
| sigLx*sigt | 1 | 1 | 0.00004937 | 0.8963 | 0.3441 |
| sigDx*sigt | 1 | 1 | 0.00003973 | 0.7212 | 0.3960 |
| sigLx*sigDx*sigt | 1 | 1 | 0.00019829 | 3.5995 | 0.0582 |
| sigDz*sigt | 1 | 1 | 0.00000620 | 0.1126 | 0.7373 |
| sigLx*sigDz*sigt | 1 | 1 | 0.00007036 | 1.2772 | 0.2588 |
| sigDx*sigDz*sigt | 1 | 1 | 0.00001916 | 0.3479 | 0.5555 |
| sigLx*sigDx*sigDz*sigt | 1 | 1 | 0.00016693 | 3.0303 | 0.0822 |
| sigeps | 1 | 1 | 0.00024273 | 4.4063 | 0.0362 |
| sigLx*sigeps | 1 | 1 | 0.00012725 | 2.3100 | 0.1290 |
| sigDx*sigeps | 1 | 1 | 0.00009545 | 1.7328 | 0.1885 |
| sigLx*sigDx*sigeps | 1 | 1 | 0.00001389 | 0.2522 | 0.6157 |
| sigDz*sigeps | 1 | 1 | 0.00003053 | 0.5542 | 0.4569 |
| sigLx*sigDz*sigeps | 1 | 1 | 0.00016663 | 3.0248 | 0.0825 |
| sigDx*sigDz*sigeps | 1 | 1 | 0.00008078 | 1.4663 | 0.2263 |
| sigLx*sigDx*sigDz*sigeps | 1 | 1 | 0.00031715 | 5.7571 | 0.0167 |
| sigt*sigeps | 1 | 1 | 0.00027739 | 5.0354 | 0.0252 |
| sigLx*sigt*sigeps | 1 | 1 | 0.00008010 | 1.4541 | 0.2283 |
| sigDx*sigt*sigeps | 1 | 1 | 0.00005828 | 1.0580 | 0.3040 |
| sigLx*sigDx*sigt*sigeps | 1 | 1 | 0.00000008 | 0.0014 | 0.9701 |
| sigDz*sigt*sigeps | 1 | 1 | 0.00008283 | 1.5037 | 0.2205 |
| sigLx*sigDz*sigt*sigeps | 1 | 1 | 0.00001119 | 0.2031 | 0.6523 |
| sigDx*sigDz*sigt*sigeps | 1 | 1 | 0.00003166 | 0.5747 | 0.4487 |
| sigLx*sigDx*sigDz*sigt*sigeps | 1 | 1 | 0.00002343 | 0.4253 | 0.5145 |

**Figure A.46:  Parameter Impact Analysis Table:  Side/Main Lobe Peak Ratio**

Response: LoLb_Pk

## Summary of Fit

| | |
|---|---|
| RSquare | 0.362574 |
| RSquare Adj | 0.333472 |
| Root Mean Square Error | 0.614357 |
| Mean of Response | 25.92303 |

## Effect Test

| Source | Nparm | DF | Sum of Squares | F Ratio | Prob>F |
|---|---|---|---|---|---|
| sigLx | 1 | 1 | 4.160825 | 11.0240 | 0.0009 |
| sigDx | 1 | 1 | 4.377057 | 11.5969 | 0.0007 |
| sigLx*sigDx | 1 | 1 | 4.313807 | 11.4293 | 0.0008 |
| sigDz | 1 | 1 | 6.236051 | 16.5222 | <.0001 |
| sigLx*sigDz | 1 | 1 | 1.730249 | 4.5842 | 0.0326 |
| sigDx*sigDz | 1 | 1 | 0.594918 | 1.5762 | 0.2097 |
| sigLx*sigDx*sigDz | 1 | 1 | 10.747993 | 28.4764 | <.0001 |
| sigt | 1 | 1 | 3.703028 | 9.8110 | 0.0018 |
| sigLx*sigt | 1 | 1 | 3.384095 | 8.9660 | 0.0029 |
| sigDx*sigt | 1 | 1 | 2.093810 | 5.5475 | 0.0188 |
| sigLx*sigDx*sigt | 1 | 1 | 5.401429 | 14.3109 | 0.0002 |
| sigDz*sigt | 1 | 1 | 3.317347 | 8.7892 | 0.0031 |
| sigLx*sigDz*sigt | 1 | 1 | 4.208996 | 11.1516 | 0.0009 |
| sigDx*sigDz*sigt | 1 | 1 | 3.323767 | 8.8062 | 0.0031 |
| sigLx*sigDx*sigDz*sigt | 1 | 1 | 4.781911 | 12.6695 | 0.0004 |
| sigeps | 1 | 1 | 5.409327 | 14.3318 | 0.0002 |
| sigLx*sigeps | 1 | 1 | 2.752783 | 7.2934 | 0.0071 |
| sigDx*sigeps | 1 | 1 | 1.698810 | 4.5009 | 0.0342 |
| sigLx*sigDx*sigeps | 1 | 1 | 5.810478 | 15.3947 | <.0001 |
| sigDz*sigeps | 1 | 1 | 7.236671 | 19.1733 | <.0001 |
| sigLx*sigDz*sigeps | 1 | 1 | 2.303503 | 6.1031 | 0.0137 |
| sigDx*sigDz*sigeps | 1 | 1 | 3.501833 | 9.2780 | 0.0024 |
| sigLx*sigDx*sigDz*sigeps | 1 | 1 | 4.163737 | 11.0317 | 0.0009 |
| sigt*sigeps | 1 | 1 | 5.692388 | 15.0818 | 0.0001 |
| sigLx*sigt*sigeps | 1 | 1 | 2.080192 | 5.5114 | 0.0192 |
| sigDx*sigt*sigeps | 1 | 1 | 0.926742 | 2.4554 | 0.1176 |
| sigLx*sigDx*sigt*sigeps | 1 | 1 | 8.132206 | 21.5460 | <.0001 |
| sigDz*sigt*sigeps | 1 | 1 | 4.599095 | 12.1851 | 0.0005 |
| sigLx*sigDz*sigt*sigeps | 1 | 1 | 3.437321 | 9.1071 | 0.0026 |
| sigDx*sigDz*sigt*sigeps | 1 | 1 | 5.277409 | 13.9823 | 0.0002 |
| sigLx*sigDx*sigDz*sigt*sigeps | 1 | 1 | 2.479491 | 6.5693 | 0.0106 |

**Figure A.47: Parameter Impact Analysis Table--Low Lobe Peak**

## APPENDIX B:  AIM INPUT FILE FORMATS AND EXECUTION

### B.1  Input Files

The AIM code requires five separate input files to perform its analysis: an "acad" input file (*.acad) that describes the geometry, a "patch" input file (*.pat) that breaks the geometry into patches, a "material" input file (*.mat) that details the transmission properties of the geometry surfaces, a "region" input file (*.reg) that lists the complex material constants of the materials within the geometry, and a global input file (*.in) that sets the various flags and parameters required by AIM to execute.

### B.1.1  ACAD Input File

Simply put, the acad input file is a collection of Cartesian points in space connected to form a 3-dimensional geometric body.  These points, called "vertices," are connected in groups of three to form "facets."  Facets are connected together to form "patches," which have identical material properties such as impedance boundary conditions.  Patches are linked together to form "segments," which are the largest building blocks of the geometric body.

For example, suppose we want to build an acad input file that describes an infinitely thin 10cm x 10cm PEC plate with a 10cm x 10cm x 10cm dielectric cube on top.  The input file "example.acad" has the format as shown below:

| | |
|---|---|
| ACAD file | !!! ACAD file designator |
| 2 | !!! Number of segments |
| Segment 1 | !!! Segment title |
| PEC plate | !!! Segment description |
| 4 | !!! Number of vertices for the plate segment |
| 0 0 0 | !!! x, y, z coordinates for vertex number 1 |
| 0 0 10 | !!! x, y, z coordinates for vertex number 2 |
| 10 0 0 | !!! x, y, z coordinates for vertex number 3 |
| 10 0 10 | !!! x, y, z coordinates for vertex number 4 |
| Patch 1 | !!! Patch title |
| 2 | !!! Number of facets-connect the vertices |
| 1 2 3 | !!! Vertices that connect to form facet number 1 |
| 2 3 4 | !!! Vertices that connect to form facet number 2 |
| Segment 2 | !!! Segment title |
| Dielectric cube | !!! Segment description |
| 8 | !!! Number of vertices for the cube segment |
| 0 0 0 | !!! x, y, z coordinates for vertex number 1 |
| 0 0 10 | !!! x, y, z coordinates for vertex number 2 |
| 10 0 0 | !!! x, y, z coordinates for vertex number 3 |
| 10 0 10 | !!! x, y, z coordinates for vertex number 4 |
| 0 10 0 | !!! x, y, z coordinates for vertex number 5 |
| 0 10 10 | !!! x, y, z coordinates for vertex number 6 |
| 10 10 0 | !!! x, y, z coordinates for vertex number 7 |

| | |
|---|---|
| 10 10 10 | !!! x, y, z coordinates for vertex number 8 |
| Patch 1 | !!! Patch title |
| 12 | !!! Number of facets-connect the vertices |
| 1 2 3 | !!! Vertices that connect to form facet # 1 |
| 2 3 4 | !!! Vertices that connect to form facet # 2 |
| 1 2 5 | !!! Vertices that connect to form facet # 3 |
| 2 5 6 | !!! Vertices that connect to form facet # 4 |
| 2 4 6 | !!! Vertices that connect to form facet # 5 |
| 4 6 8 | !!! Vertices that connect to form facet # 6 |
| 3 4 7 | !!! Vertices that connect to form facet # 7 |
| 4 7 8 | !!! Vertices that connect to form facet # 8 |
| 1 3 5 | !!! Vertices that connect to form facet # 9 |
| 3 7 8 | !!! Vertices that connect to form facet # 10 |
| 5 6 7 | !!! Vertices that connect to form facet # 11 |
| 6 7 8 | !!! Vertices that connect to form facet # 12 |

Note that comments to the right of exclamation points are ignored by the AIM code.

Four important points about the creation of ACAD files and their interpretation by the computational electromagnetics code must be made.

First, there are general rules of vertices per wavelength that each CEM code must follow to retain accuracy. This is due to the fact that the codes are solving for surface currents

using sub-domain basis functions, and are attempting to fit those functions along the triangles bounding each edge. If the vertices describing a triangle are too far apart, the basis functions begin to fit multiple modes on the same line and thus, accuracy is decreased. AIM gives a rule of thumb of eight vertices per wavelength; for the ACAD file above, this would restrict us to operating frequencies of 3.75 GHz or below.

Second, the facets on the geometry should be both optimally spaced with relation to each other, and with relation to the geometry. Triangular facets should be as close to equilateral triangles as possible; this ensures the maximum coverage for the minimum number of facets. Also, facets should be more concentrated in known regions of rapid field variation, such as edges or corners, since this is where the surface currents will build up.

Third, each triangular facet must have no more than three nodes along its edge. The sub-domain basis functions cannot fit properly along edges with multiple nodes, and most codes will ignore the facet completely and return an error message.

Lastly, vertices must never be duplicated along shared edges. This can sometimes occur when the user creates different segments separately and then attempts to patch them together into a single body. Some CEM codes cannot rectify multiple nodes designated along the same edge, and will fail to connect the geometry as the user would like.

B.1.2  Patch Input File

The patch input file designates the material regions above and below each patch, and the impedance boundary conditions (if any) for each patch. The "m#" entry denotes the impedance boundary material number, as listed in the material input file. The "r-" and "r+" entries designate the material region on the "negative" and "positive" sides of the surface, respectively. Direction is defined using the right-hand rule as follows: the right hand should sweep in the direction of increasing vertex number when defining facets. In our example, the first facet of our PEC plate is made by linking vertices 1, 2, and 3. Sweeping the right hand in the direction of increasing vertex number gives us a "positive" side of the PEC surface next to the dielectric cube. The "s-patch" entries denote which patches belong to a larger entity called a "superpatch," which can be created when junctions between different surfaces must be linked together. In our example, we assume that all surfaces are perfectly transmissive and thus, each patch is its own superpatch.

Below is the patch input file that corresponds to our example, "example.pat". Once again, comments to the right of exclamation points are ignored by the code.

```
! example.pat
1                                           !!!   Segment 1, the PEC plate
!<-patch   m#   r-   r+   s-patch->                Dielectric region on
!                                                 positive side,
1          0    0    1    1                  !!!   free space on negative side.
2                                           !!!   Segment 2, dielectric cube
```

| !<-patch | m# | r- | r+ | s-patch-> | !!! | Free space on the |
| --- | --- | --- | --- | --- | --- | --- |
| ! | | | | | | positive side, |
| 1 | 1 | 0 | 0 | 1 | !!! | free space on the negative |
| ! | | | | | | side |

## B.1.3 Material input file

The material input file describes the transmissive properties of the surface of each patch in terms of the electrical resistivity R, magnetic resistivity S, and cross resistivity U. Since we are assuming that all patches are completely transmissive, we assign values of 100000 (an approximation to infinity) to the real parts of R and S. The first row contains the file name; the second row is the number of patch surfaces described in the file. The third and following rows give the real and imaginary parts of R, S, and U for each surface:

example.mat

| ! | Real R | Imag R | Real S | Imag S | Real U | Imag U |
| --- | --- | --- | --- | --- | --- | --- |
| 1 | | | | | | |
| 2 | 100000 | 0 | 100000 | 0 | 0 | 0 |

## B.1.4 Region Input File

The region input file lists the volumetric material constants of the materials contained within the geometry, using complex ε and complex μ. The following region file lists the parameters for our single non-PEC region, the dielectric cube:

example.reg

| ! | Real Eps | Imag Eps | Real Mu | Imag Mu |
|---|----------|----------|---------|---------|
| 1 |          |          |         |         |
|   | 4        | 0        | 1       | 0       |

## B.1.5  Global Input File

The global input file lists files and sets parameters that the AIM code requires to run. Although there are many flags that can be set, only the required inputs are set in the following example input file, named "example.in":

| geofile exampleD1.ced | !!! | These are geometric files produced |
|------------------------|-----|-------------------------------------|
| dgeofile        exampleD1.ced | !!! | by the JREG and GDOMS utilities. |
| a_file   example | !!! | Filename for intermediate files |
| alam    80.0 | !!! | Wavelength, in terms of ACAD units |
| thi      0 1.0 90 | !!! | Incident theta (initial, incr, final) |
| phi      90 0 90 | !!! | Incident phi (initial, incr, final) |
| poli     v | !!! | Incident polarization |
| it_mem        500 | !!! | Max # of trial solutions to be |

!!!      stored in memory

## B.2 Diagnostic Utilities:  ADISP and GGINFO

The AIM package has two diagnostic tools that ensure the ACAD files can be read by the
AIM program.  ADISP is a display program that can display ACAD files or processed
CED files, including all of the vertices, edges, and facets that make up the ACAD
geometry.

GGINFO is a utility that checks the vertices, facets, patches, and segments of the ACAD
file to verify that they are properly connected, and tells the user where any errors in the
ACAD file are located.

## B.3 Pre-processing Utilities:  JREG and GDOMS

The input files above are processed by the JREG and GDOMS utilities and converted into
a unified file format readable by the AIM code.

The JREG utility joins the material regions into an intermediate geometry file, designated
with a ".ced" extension.  It requires the material input file, the patch input file, and the
acad input file and uses the following UNIX command line:

```
jreg -p example.pat -m example.mat -o example.ced example.acad
```

The following is the output on the screen:

```
surface --> segment

      1 -->        1

      1 -->        2

Reassigned 18 edges.

files: example.acad example.pat example.mat --> example.ced
```

The GDOMS utility takes the output file from the JREG utility and converts it to a domain decomposed file, depending on the number of domains the user wishes to divide the AIM computation into for purposes of parallel processing.  For this example, we set a single domain for sequential AIM operations with the following command line:

```
gdoms example.ced
```

The following is displayed on the screen:

```
input: v-e+f:     24 -     46 +     28 =      6  e_in:      38 e_0:

1 nonempty domain

object  pos:  (    0.000000      0.000000      0.000000)

object size:  (   10.000000     10.000000     10.000000)

domain size:  (   10.001000     10.001000     10.001000)

        v-e+f:     24 -     46 +     28 =      6  e_in:      38 e_0:

r:   *  $

                                total:  e_in:      38 e_0:

                                  min:              38
```
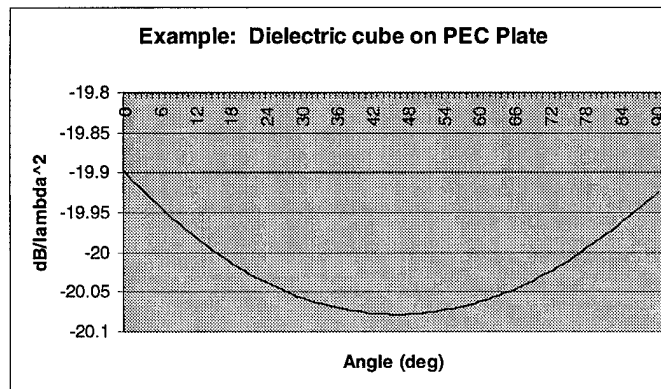
```
                                        max:            38

                                        av:             38
files: example.ced --> exampleD1.ced
```

## B.4  AIM Execution and Output

The AIM code requires the following command line to execute, which takes the global

input file "example.in" and pipes the output into "example.out":

aim64 example >& example.out

The following is a plot of the example.out output file, plotting dB per square wavelength

vs. angle.



**Figure B.1:  Dielectric cube/PEC plate output**

## APPENDIX C: MSRC DOCUMENTATION

## C.1  MSRC Overview

The Aeronautical Systems Center Major Shared Resource Center (ASC MSRC) is a part of the Department of Defense (DOD) High Performance Computing Community. The ASC MSRC is physically located in Area B, Building 676, of Wright-Patterson Air Force Base (WPAFB), near Dayton Ohio.

The ASC MSRC is comprised of commercial and "in-house" developed scientific and engineering application software, combined with the hardware needed to support those applications. It also includes methodologies to configure and use these resources in a simple and standardized manner.

The ASC MSRC contains a variety of application and file servers. It supports X-windowing devices to facilitate graphical user interfaces (GUIs) in accessing the available computational resources and to perform Scientific Visualization. On-line archival storage is also available.

## C.2 SGI Origin 2000 Overview

The Origin 2000 has a total of 224 CPUs. Each CPU is an 195 MHz R10000 MIPS processor with a peak speed of 400 MFLOPs, providing a total capacity of approximately 90 GFLOPs. Each CPU has a primary data cache of 32 Kb, a primary instruction cache of 32 Kb, and a secondary cache of 4 Mb. At this time, the Origin 2000 is divided into 7 separate systems. Each of these systems has 32 CPUs, 16 GBytes of memory, and 70 GBytes of workspace. The Origin 2000 has a SMP architecture which allows each CPU full access to the total amount of memory on each system [Lucas].

## C.3 Batch job submission

Users of the SGI Origin 2000 machine are required to use the Portable Batch System (PBS) for batch job submission. This is required for any job lasting more than fifteen minutes, since jobs running beyond fifteen minutes in the interactive mode are automatically killed.

The following is a sample batch job script used to run the "example" case outlined in Appendix B:

```
#! /bin/csh
#PBS -q  default
#PBS -l ncpus=4
#PBS -l pcput=1:00:00
#PBS -l cput=1:00:00
```

```
#PBS -l pmem=10MW
#PBS -l mem=10MW
#PBS -N example_O2k
#PBS -o example_O2k.output
#PBS -e example_O2k.err
#PBS -S /bin/csh
#PBS -r y
#    Set environment
setenv ExecHost `hostname`
#    Change to WRK
set echo
cd $WRK
#    Copy input and program from users HOME directory
cp $HOME/exampleD1.ced example.reg $WRK
cp $HOME/example.in example.mat aim64 $WRK
#    Check Exechost and rcp if necessary
if ( $ExecHost != hpc03-1 ) then
  /usr/bsd/rcp hpc03-1:$WRK/exampleD1.ced example.reg .
  /usr/bsd/rcp hpc03-1:$WRK/example.in example.mat aim64 .
endif
#    Run the program
aim64 example >& example.out
#    Copy output to home directory
cp example.out $HOME
#    Check Exechost and rcp if necessary
if ( $ExecHost != hpc03-1 ) then
  /usr/bsd/rcp example.out hpc03-1:$WRK
endif
#    Clean up WRK directory
rm example.*
rm exampleh.*
#    End script
```

# BIBLIOGRAPHY

Anderson, L. W. *Introduction to PMM*, Technical Report 715582-5, ElectroScience Laboratory, Ohio State University, generated under contract F33615-83-C-1024, for Avionics Laboratory, Air Force Wright Aeronautical Laboratories, Wright-Patterson AFB, Ohio, February 1986.

Bleszynski, Elizabeth; Bleszynski, Marek. *Development and Implementation of Computational Electromagnetic Techniques on Massively Parallel Structures, Volumes 2 and 3, Phase II: User's Manual and Installation Guide*, WL-TR-97-6009, Boeing Information, Space and Defense Systems and Rockwell Science Center, generated under contract F-33615-93-C-1350, for Avionics Laboratory, Air Force Wright Aeronautical Laboratories, Wright-Patterson AFB, Ohio, July 1997.

Balanis, C. A. Advanced Engineering Electromagnetics. New York: John Wiley and Sons, 1989.

Brown, F. B.; Sutton, T. M. *Monte Carlo Fundamentals*, Technical Report KAPL-4823, Knolls Atomic Power Laboratory, generated under contract DE-AC12-76-SN-00052, for the Department of Energy, February 1996.

Chavez, Edwin V. "Manufacturing tolerance requirements for Frequency Selective Surfaces," M. S. Thesis, Air Force Institute of Technology, 1993.

Collins, Peter J.; Skinner, J. Paul. Course notes for EENG 727, "Frequency Selective Surfaces." Department of Electrical and Computer Engineering, School of Engineering, Air Force Institute of Technology, Wright-Patterson AFB, OH, July 1997.
Fishman, George S. Monte Carlo--Concepts, Algorithms, and Applications. New York: Springer-Verlag, 1996.

Godsey, James A. "Tolerance Theory of Periodic Surfaces," Dissertation, Air Force Institute of Technology, 1995.

Greene, William H. Econometric Analysis. New York: Macmillian Publishing Company, 1993

Hendrix, Jennifer Morison (ed.) Microsoft Office 97 Resource Kit. Washington: Microsoft Press, 1997.

Hill, Roger A.; Munk, Benedikt A. *The effect of perturbating a frequency-selective surface and its relation to the design of a dual-band surface*, IEEE Transactions on Antennas and Propagation, vol. 44, p. 368-374, March, 1996.

Koleck, T.; Diez, H.; Bolomey, J. C.; Mittra, R. A technique for analyzing finite frequency selective surfaces, IEEE Antennas and Propagation Society International Symposium 1997, vol. 4, p. 2372-2375, July 1997.

Lucas, Cheryl; McLean, Deborah (ed.) "ASC MSRC Journal," volume 1.2, Fall 1997.

Luebbers, R. J.; Munk, B. A. *Some effects of dielectric loading on periodic slot arrays*, IEEE Transactions on Antennas and Propagation, vol. AP-26, no. 4, p. 536-542, July 1978.

Montgomery, Douglas C. Design and Analysis of Experiments. New York: John Wiley & Sons, 1976.

Munk, B. *Theory and Applications of Frequency Selective Surfaces (FSS) to Electromagnetic Radiation and Scattering Problems: A Short Course*, Technical Report AFWAL-TM-86-1-AAWP, for Avionics Laboratory, Air Force Wright Aeronautical Laboratories, Wright-Patterson AFB, Ohio, March 1986.

Press, William H.; Flannery, Brian P.; Teukolsky, Saul A.; Vetterling, William T. Numerical Recipes in C. Cambridge: Cambridge University Press, 1988.

SAS Institute, INC. JMP User's Guide. Cary, NC: SAS Institute INC, February 1995.

Skinner, J. Paul. "Scattering from a Finite Collection of Transverse Dipole and Axial Slot Arrays with Edge Effects," Ph. D. Dissertation, Ohio State University, 1991.

Taylor, John R. An Introduction to Error Analysis. University Science Books, 1982.

Utt, Edwin L. Telephone Interview, conducted by Matthew D. Craig at Wright-Patterson AFB, OH, January 1998.

# VITA

Matthew D. Craig received a Bachelor's of Science in physics from Michigan State University in May 1994. He completed the AFROTC program as a Distinguished Graduate at Detachment 380, Michigan State University, and was commissioned into the U.S. Air Force. In September 1994 he was assigned as a developmental engineer to the Phillips Laboratory Propulsion Directorate at Edwards AFB, where he was responsible for conducting live-fire testing of solid rocket motors to support new propellant development. He was married in August 1995, and in August 1997 he was assigned to the electrical engineering department at AFIT as a Master's degree student specializing in low observables. His follow-on assignment is at AFRL/XPN, located at Wright-Patterson AFB.